Temperature Variability in Narragansett Bay: Integrating Four Decades of Remote Sensing Observations and In-situ Sea Surface Measurements

Ashfaq Ahmed[1], Baylor Fox-Kemper[2], Daniel Wexler[2], and Monica M. Wilhelmus[1]

[1]Center for Fluids and Thermal Science, Brown University
[2]Department of Earth, Environmental, and Planetary Sciences, Brown University

Key Points:

- This study integrates a 39-year-long multi-satellite Landsat temperature record with in situ field buoy measurements and tide records for analyzing seasonal, annual, and interannual sea surface temperature (SST) variability in two tidal estuaries on Rhode Island (Narragansett Bay and Mt. Hope Bay).
- The first two empirical orthogonal modes explain 79% of Narragansett Bay and 87% of Mt. Hope Bay SST variability and are dominantly seasonal in time.
- The SST variability of these estuaries is significantly larger than the one pertaining to the ocean shelf.

Corresponding author: Monica M. Wilhelmus, mmwilhelmus@brown.edu

Abstract

Characterizing sea surface temperature (SST) variability is critical for understanding long-term changes in estuarine environments. In this study, we presented the first analysis of the 39-year-long SST evolution in Narragansett Bay by combining remote sensing records and in-situ measurements. Using multi-satellite Landsat data ($\sim$ 15 day sampling), in-situ buoys (15 min. sampling), and tide gauges (60 min. sampling), we retrieved the seasonal-to-decadal sea surface and tidal temperature variabilities and trends over four decades in Narragansett Bay and its arm Mt. Hope Bay. We used pattern recognition techniques like Empirical Orthogonal Function and showed that the seasonal solar heating and bathymetry determine dominant ($\sim$ 80%) temperature variance in the bay. We found the annual mean SST warming trend to be $0.061 \pm 0.024\,^{\circ}\mathrm{C\,yr^{-1}}$ and $0.041 \pm 0.018\,^{\circ}\mathrm{C\,yr^{-1}}$ for Narragansett Bay and Mt. Hope Bay, respectively. While Landsat sampling is too infrequent to track tides, composites of Landsat images constructed the SST distributions for each tidal phase. High-frequency measurements reveal that tidal temperature changes are predominantly influenced by vertical mixing, with the shallower upper bay showing greater SST variability than the lower bay. Importantly, we anticipate our study to represent the synergic advantages of utilizing Landsat and in-situ buoy data to offer new and deeper insights into the changing conditions of the global estuaries.

1 Introduction

Sea surface temperature (SST) is a primary indicator of biochemical activities, physical processes, and climate systems within an estuary (Bertram et al., 2001; Oviatt et al., 2002; Hu et al., 2020; Wang et al., 2021; Rubinetti et al., 2022). SST influences the metabolism and productivity of estuarine marine life; rising SSTs are understood to contribute to global-scale eutrophication (L. Li et al., 2021; Xu et al., 2022). Any abrupt shifts in the water temperature in shallower estuaries can significantly harm critical life cycle events (e.g., larval development, spawning, plankton bloom) of aquatic organisms (Paxton et al., 2016; Priyanka et al., 2021). Estuarine water with shallow bathymetry exhibits significant temperature fluctuations between seasons (Oczkowski et al., 2015). In addition to that, seasonal changes in SST can significantly affect the water chemistry, nutrient transport, and the movement of pollutants (McLusky et al., 1986; Leal Filho et al., 2022). Beyond its role in biochemical processes, SST stands as a notable driver of estuarine atmospheric dynamics (McGrath et al., 2008; Pourkerman et al., 2023). Elevated SST leads to higher evaporation rates, enhanced local humidity and precipitation, and can form low-level clouds (Guo et al., 2022). Multiple factors can contribute to changes in estuarine water surface temperature, including impervious surface runoff (Barlage et al., 2002), climate change (Kennedy, 1990; Brown et al., 2016), complex bathymetry (Simionato et al., 2010; Vroom et al., 2017), and anthropogenic activities (Cloern et al., 2016; Kennish, 2019).

Since the beginning of the satellite era nearly six decades ago, the spatial and temporal resolution of SST measurements from remote sensing has improved dramatically (O'carroll et al., 2019; Minnett et al., 2019; Lloyd et al., 2021). Yet, satellites designed to cover vast areas (e.g., Advanced Very High-Resolution Radiometer, with $\sim$ 1 km spatial resolution) often fall short in capturing oceanographic changes that occur on short time scales near the coastlines (i.e., tide, storm surges, and waves). One effective way to address this limitation is to combine satellite images with in-situ sensors, such as fixed buoys, autonomous floats, and ship-based measurements. This combination facilitates the accuracy and reliability of coastal satellite measurements to track the short-term influences of tides (Adebisi et al., 2021), offshore water salinity and turbidity (Zhao et al., 2017), estuarine plumes (C. Li et al., 2017), clouds (Wojtasiewicz et al., 2018), under-water topography (Fassoni-Andrade et al., 2021), and thermal effluents (Benoit & Fox-Kemper, 2021).

In coastal regions like Narragansett Bay, while in-situ measurements are favored for their precision and real-time insights (Goetz et al., 2009; Turner et al., 2015), they come with challenges. They often fall short in providing extensive spatial coverage, which limits their effectiveness for large-scale assessments. Furthermore, deploying and maintaining in-situ instruments, especially in harsh or remote locations, is costly and logistically taxing (Ibrahim & Samah, 2011; Jeong et al., 2016). To overcome these limitations, we adopted a hybrid approach, merging satellite and in-situ records to analyze four decades of estuarine sea surface temperature dynamics in Narragansett Bay.

Previous studies made efforts to explain the evolution in the SST distribution patterns of Narragansett Bay to describe its underlying estuarine climatology (Carney, 1997; Nixon et al., 2003; Fox et al., 2005; Smith et al., 2010). Based on an analysis of 53 Landsat scenes from 1984 to 2002, Fisher and Mustard (2004) pointed out that shallow-water bodies in Southern New England exhibit more extreme temperature variations (-2 to 25°C) compared to deeper water bodies (4 to 18°C). Benoit and Fox-Kemper (2021) utilized statistical techniques to evaluate the temperature distribution and spatial pattern of thermal effluent generated by the Brayton Point Power Station. The present study extended Benoit and Fox-Kemper (2021) and outlined a deeper understanding of SST patterns shown through continuous monitoring of the entire Narragansett Bay. We utilized high-quality, in-situ calibrated, multi-decadal multi-satellite Landsat data on Narragansett Bay and its neighboring Mt. Hope Bay. Our study detailed the high-resolution spatial (Landsat) and temporal (buoy data) patterns of SST variability, including the M_2 tidal signal composites over the last 39 years. We computed within clouds and artifacts using mathematical frameworks like the empirical orthogonal function (EOF). Then, we formed EOF patterns from the continuous cloud-free record to interpret the dominant spatial and temporal modes of seasonality. Finally, we utilized two different approaches to assess the ability of Landsat, with its low sampling rate, to capture the high-frequency tidal temperature anomalies in the bay in all four tidal phases.

This paper is organized as follows. Section 2 and Section 2.1 describe the study area and the key estuary variabilities of Narragansett Bay. Sections 3.1, 3.2, and 3.3 provide a detailed description of the data, while Section 4 discusses the general methodology of the paper. The final results and discussion are presented in section 5. We concluded the writing with a complemented forward-looking perspective on enhancements and possible uses of the techniques we applied in this paper.

2 Study Area

Narragansett Bay spans 328 km^2, constituting the largest estuary in New England (Figure 1, panel a). A five-river system provides the bay with a total freshwater influx of $105\,\mathrm{m^3\,s^{-1}}$, further augmented by an additional $37\,\mathrm{m^3\,s^{-1}}$ from annual rainfall reaching approximately one meter (Fox et al., 2000). Its dynamic watershed generates a distinct salinity front where river water meets the open ocean and forms a freshwater plume that extends to Rhode Island Sound. Narragansett Bay watershed fosters a rich diversity of plant and marine animal species (Raposa, 2009; Byron et al., 2011). From an economic standpoint, this region serves as home to over two million residents in Rhode Island and Massachusetts and plays a key role in sustaining the blue economy of this region of the United States (Oviatt et al., 2003; Alves, 2007).

2.1 Estuary Variabilities: Narragansett Bay

Narragansett Bay is particularly susceptible to climate change, given its vicinity to the Gulf of Maine in the North Atlantic. According to Mills et al. (2013), the water temperature of the Gulf of Maine has been increasing at one of the quickest rates compared to the global ocean. Several recent studies have drawn increased attention to the repercussions of this trend. For example, Pershing et al. (2021) noted that the increased temperature in the Gulf of Maine has profound impacts on the climatology and ecosystem of the broader North Atlantic (i.e., enhanced water column stratification, decrease in the surface salinity and increase in algal bloom). As pointed out by Hurrell and Deser (2010), the prolonged positive phase of the North Atlantic Oscillation is also linked to the recent rising levels of greenhouse gases and decreased amounts of stratospheric ozone in the atmosphere. The influence of short-term climate shifts is also important. For instance, predictions from the high-resolution climate models reported pronounced warming of the Northwest Atlantic as the CO_2 levels doubled over the last 70-80 years (Saba et al., 2016).

The local weather and SST patterns in Narraganset Bay are predominantly affected by solar radiation (Mustard et al., 2001), estuarine flows (Geyer & MacCready, 2014), and tidal cycle (Bowers & Brubaker, 2021). Typically, the water surface temperature of the bay oscillates between -2°C and 25°C (Fisher & Mustard, 2004) throughout the year. However, the northern segment of the bay is exposed to more extreme temperature changes between seasons due to its shallower bathymetry. In Narraganset Bay, the semi-diurnal M_2 tide plays a crucial role in the tidal circulation and contributes to 80% of the total current energy (Kincaid, 2006). The sea level elevation in the bay typically oscillates between 0.06 to 1.6 m with an average flushing time of 26 days. Wind-driven variability has also been shown to influence the changes in SST in Narragansett Bay (Pfeiffer-Herbert et al., 2015). Wind can potentially mix the entire column of shallow waters and promote uniform temperature changes. In contrast, deeper waters resist rapid shifts due to their higher thermal inertia and stratification. Finally, low-frequency river variability dominates sea surface salinity in models of summertime conditions—to the extent in which responses to individual force agents can be quantified (Sane et al., 2023).

3 Data

3.1 Landsat Data

Satellite remote sensing instruments are frequently used to monitor the physical features of estuaries. Examples include the Moderate Resolution Imaging Spectroradiometer (MODIS), the Medium Resolution Imaging Spectrometer (MERIS), and the Geostationary Ocean Color Imager (GOCI) sensors (Kilpatrick et al., 2001; Fournier et al., 2015; Barnes & Hu, 2016; Sathyendranath et al., 2019; Zeng et al., 2020). Satellite instruments typically are an excellent complement to field observations because of their high spatial coverage (Sandau et al., 2010; X. Li et al., 2019; Rivas-Fandiño et al., 2023). However, satellite data is usually acquired with a coarse spatial resolution (frequently 1 km), which limits their applicability for analyzing intricate estuarine systems such as Narragansett Bay (McPherson et al., 2006).

NASA's Landsat program has acquired the longest continuous record of Earth at high resolution (30-120 m). While most of the Landsat record documents land resources (i.e., vegetation, wildfire, and biomass changes), the thematic mapper (TM) and thermal infrared (TIR) sensors can be effectively used to measure local SST on coasts (Tarantino, 2012; Jaelani & Alfatinah, 2017; Fu et al., 2020). These spectral bands can pixel-wise detect and convert the heat radiation emitted by the sea surface into temperature values (Reddy, 2018; Vanhellemont et al., 2022). Using Landsat to measure SST has some challenges. For instance, atmospheric conditions can compromise the accuracy of the temperature reading, and the sampling rate might not be sufficient to retrieve small-scale variability in coastal regions. Nonetheless, each successive iteration of Landsat (i.e., Landsat 5, 7, 8) offers enhanced spatial resolution, more spectral bands, and improved calibration (Roy et al., 2016), which make them more efficient in capturing fine-scale details in an estuarine setting.

In our study, we collected images from the USGS EarthExplorer (`https://earthexplorer.usgs.gov`) multispectral Collection 2 Level 2 processed GeoTIFF Data Products from Landsat 5, 7, and 8 satellites. The product included calculated brightness temperature values for the thermal bands of each satellite. We defined the study area by the rectangular bounding box that intercepts 990 Landsat scenes from Path 12, Row 31 of the WRS 4/5 coordinate system. Each satellite samples every 16 days in sync with the sun. However, the presence of clouds often blocks the view and extends the delay between scenes. Therefore, from the initial pool, we only kept 764 scenes with less than 50% cloud coverage over Narragansett Bay, with an average sampling interval of 18.375 days (or 441 hours). Before any analysis, we eliminated the interference from land and clouds (sections 4.1, 4.2) with a series of processing steps. We applied land mask and cloud quality attributes to ensure the reliability of the SST analysis following Hansen et al. (2013). Thus, we adjusted all bands for atmospheric correction, with units expressed as reflectance, while the thermal band provided values in Kelvin.

3.2 RIDEM Buoy Data

A collaborative effort to assess the water quality among multiple organizations established a comprehensive monitoring station network overseen by the Rhode Island and Massachusetts Departments of Environmental Management (RIDEM, MADEM). We used water surface temperature (°C) data from these monitoring stations for this study. These stations are strategically positioned across the bay and continuously record water quality parameters at 15-minute intervals. Our study focused solely on the data obtained from RIDEM, which covers 13 locations within Rhode Island. We have omitted buoy data from the MADEM, which has only been installed recently. The monitoring stations span the estuary from near river mouths through the freshwater-marine mixing zone (Figure 1, panel a). The buoy data collection period ranges from 2003 to the present. Not all buoys are year-round; the data predominantly focus on the spring to fall seasons, resulting in a calibration that may be biased toward the summer months.

3.3 NOAA Tide Data

The Tides and Currents program, administered by the National Oceanic and Atmospheric Administration (NOAA), provides sea level elevation (in meters) data spanning from 1984 to 2022. For this study, we collected hourly sea level elevation data from station 8447386 Fall River, MA, and in station 8454658 Narragansett Pier, RI (see Fig. 1, panel a).

4 Method

In this section, we present the data analysis tools used for Landsat (Bias Correction, Cloud In-Filling, EOFs) and applied to both buoys and Landsat (detrending, Lomb-Scargle power spectra).

4.1 Bias Correction

Landsat and buoys may record temperatures at different times, so it is important to adjust the temporal sampling. The long-wavelength Landsat thermal bands have a restricted penetration depth into water (approximately 10 µm). Therefore, the bands predominantly represent the thermal signal of the water skin. On the contrary, RIDEM buoys are generally installed at depths ranging from 0.5 to 1.0 m below the water surface. Although under exceptionally calm conditions, both satellite and on-site measurements in-

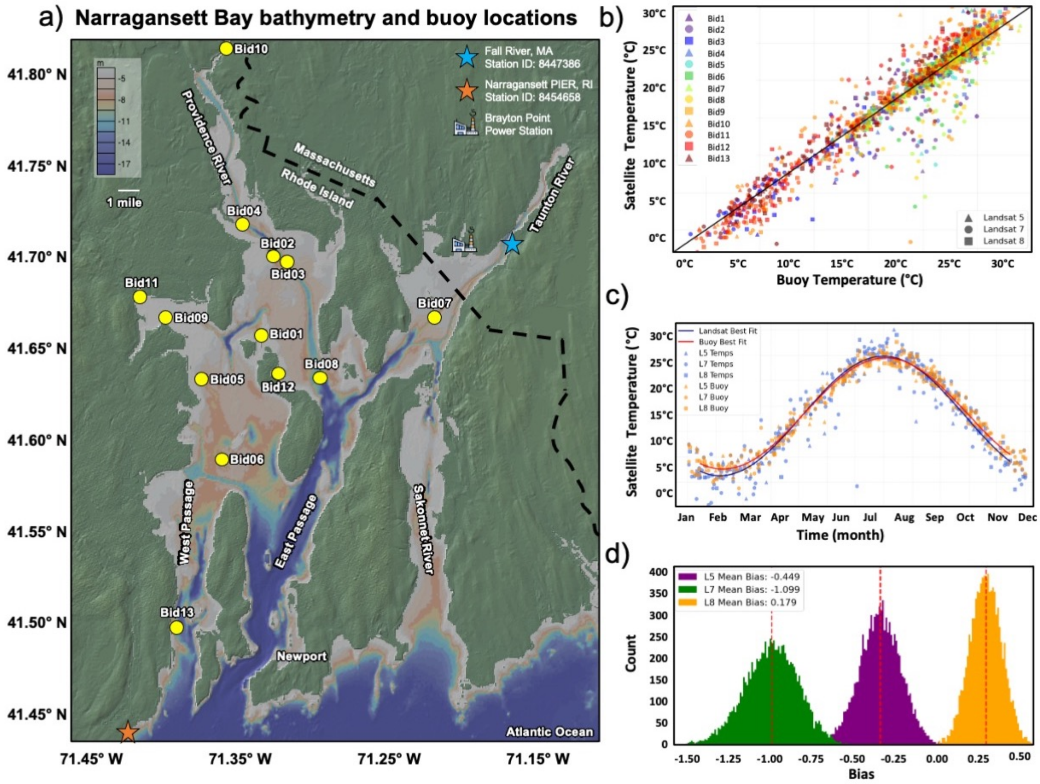

Figure 1. a) The spatial arrangement of the 13 monitoring buoys established by the RIDEM and the NOAA tide gauge locations within Narragansett Bay are presented. The bathymetry data of the bay is collected following the work of Ryan et al. (2009). b) The process of preparing the in-situ corrected Landsat satellite data before cloud in-filling is illustrated, showing a good alignment (compared to a 1:1 relationship) between the buoy temperatures and the calibrated satellite temperature. c) A typical temperature climatology of the Bay is presented, providing a comprehensive overview of the temperature variations throughout the year. d) The spread of sample bias for all three satellites indicates the systematic biases and typical near-Gaussian spread between the satellite-derived temperatures and the buoy measurements.

Table 1. Information about the Landsat satellites

Satellite	Band	λ (μm)	Pixel	Calculated Bias (°C)	Period
L5	TM	10.40-12.50	60m	-0.45	1984-2011
L7	TM Band 6	10.40-12.50	60m	-1.094	1999-present
L8	TIRS	10.60-11.19	100m	0.178	2013-present

dicate similar temperatures due to typical surface mixing, their measurements might differ in regions characterized by limited mixing (Schneider & Mauser, 1996). To minimize this difference, we employed a bias correction technique with specific corrections tailored to each generation of Landsat, as detailed in Table 1.

In reality, the temporal sampling resolutions differ significantly between the satellite images (approximately 18.375 days) and the buoys (every 15 minutes). To avoid momentary anomalies, we took the average of five buoy readings closest to the time a satellite image is captured, following the approach of Benoit and Fox-Kemper (2021). Next, we aligned the satellite metadata dates with the buoy data to sync the two SST records. This revised dataset includes Landsat measurement dates and SST values collected from all thirteen buoys between 2003 and 2022.

Once the sampling times from Landsat and buoys were adjusted, we accurately matched their corresponding pixels. First, we used a land mask to remove all the land pixels. Then, we removed any cloud structures from the satellite images using cloud masks as described by Benoit and Fox-Kemper (2021). Specifically, for Landsat 5 and 7, we masked clouds and cloud shadows. As for Landsat 8, we additionally masked cirrus clouds because the metadata for cirrus clouds is unavailable for Landsat 5 and 7. We took into consideration that the buoys may move slightly due to tidal effects and seasonal adjustments in their anchoring. Therefore, we computed a spatial average within a 200-square-meter zone around each of the 13 standard buoy spots. This process results in a final dataset that includes the Landsat recording dates and the spatially averaged SST values at the buoy sites, covering the period from 2003 to 2022.

The adjustments of both temporal and spatial sampling metrics set the ground for us to apply the bias correction and linear re-scaling. We completed the calibration without overfitting and followed the methodology of Benoit and Fox-Kemper (2021) for each Landsat satellite and the corresponding buoy temperature. We gathered the temperature differences between the mean SST record of all thirteen buoys and the corresponding spatially averaged satellite measurements. At this step, we removed the mean biases over the lifetime of each satellite from the Landsat records at all locations (Table 1). The removal of the mean biases generated a collective dataset of buoy-calibrated Landsat temperatures spanning from 1984 to 2022 (Fig. 1, panels b, c, and d). It should be emphasized that the buoy data covers 2003 to 2022, so the calibration was limited to this timeframe. Additionally, we are highlighting that only Landsat 5 provided satellite scenes before 1999, and the paucity of observation limited the total number of available scenes. However, the launches of Landsat 7 in 1999 and Landsat 8 in 2013 added more frequent observation in the later years.

4.2 Cloud In-filling

Satellite image cloud in-filling is a technique for restoring missing data in satellite images caused by cloud cover (Wulder et al., 2011). Cloud in-filling employs surrounding pixel information and patterns of observed variability in the exact location across the dataset and estimates values for obscured pixels. This technique can facilitate the generation of continuous and uninterrupted sea surface temperature maps (Lindquist et al., 2008; Roy et al., 2010). Narragansett Bay is susceptible to persistent cloud cover because of frequent weather fluctuations and cold air interacting with the temperate water south of Cape Cod. Hence, satellite observations of the bay can be interfered with, particularly during the fall and summer months when cloud cover is more prevalent (Dalton et al., 2010).

Landsat does not penetrate clouds, so in order to use infilling and pattern recognition approaches, it is necessary to attribute SST where clouds are overhead. We used the EOF-based approach of Data Interpolating Empirical Orthogonal Functions (DINEOF) algorithm (Beckers & Rixen, 2003; Alvera-Azcárate et al., 2011) to impute the missing (cloud-covered) pixels in the bias-corrected data from May 1984 to September 2022. To estimate errors, we added synthetic clouds at random locations over the bay and compared the filled-in values to the true values (see Table 2).

Table 2. Statistics for likely error in each infilled data point, based on tests using synthetic clouds of withheld data.

Mean	Standard Deviation	Skewness	Kurtosis
0.670	3.277	1.252	6.550

4.3 EOFs of the Bay

Empirical Orthogonal Function (EOF) analysis identifies dominant variability patterns in multivariate datasets (Weare & Nasstrom, 1982; Chen & Harr, 1993; Hannachi et al., 2007; Navarra & Simoncini, 2010). We employed the EOF technique to explore the dominant temporal and spatial SST patterns in Narragansett Bay. Section 5.1 provides a comprehensive explanation of the long-term general SST patterns of the bay. In this section, we outlined the matrices preparation for the input data into the EOF algorithm.

To consider the time correlation of the SST for both bays, we can write -

$$M_{\text{Narragansett Bay}} = SST_1 \tag{1}$$

$$M_{\text{Mt. Hope Bay}} = SST_2 \tag{2}$$

Where,

$$SST_1 = \begin{bmatrix} x_{1,1} & x_{1,2} & x_{1,3} & \dots & x_{1,j} \\ x_{2,1} & x_{2,2} & x_{2,3} & \dots & x_{2,j} \\ \vdots & \vdots & \vdots & \ddots & \vdots \\ x_{i,1} & x_{i,2} & x_{i,3} & \dots & x_{i,j} \end{bmatrix} \tag{3}$$

$$SST_2 = \begin{bmatrix} x_{1,1} & x_{1,2} & x_{1,3} & \dots & x_{1,n} \\ x_{2,1} & x_{2,2} & x_{2,3} & \dots & x_{2,n} \\ \vdots & \vdots & \vdots & \ddots & \vdots \\ x_{m,1} & x_{m,2} & x_{m,3} & \dots & x_{m,n} \end{bmatrix} \tag{4}$$

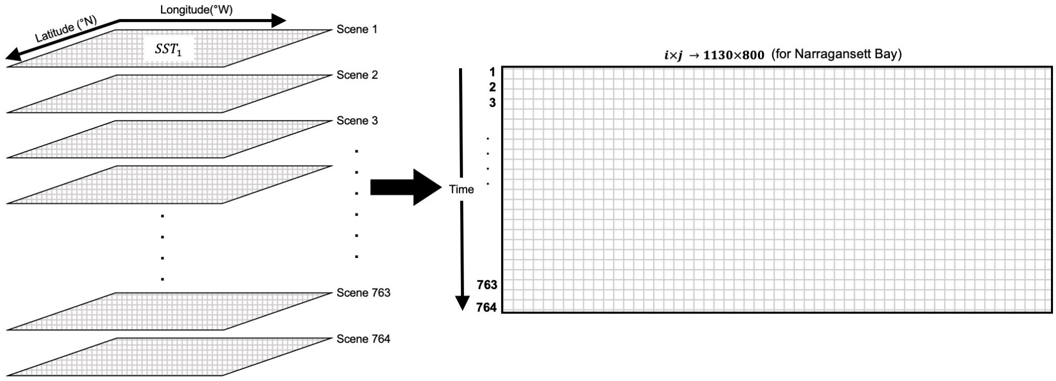

Figure 2. (Left) Representation of grid cell information from the 3D data stack for Narragansett Bay temperature matrix. (Right) Each row of the transformed 2D matrix contains all pixel information from a single scene, with spatial information spread across each row and temporal information across each column.

For each scene, the pixel temperature information is denoted as x, which is a function of time. The total count of spatial grid points for Narragansett Bay is indicated by i and j, while for Mt. Hope Bay, it is denoted by m and n. Both SST_1 and SST_2 are three-dimensional matrices, and the third dimension refers to the evolution of the scenes with time (see Fig. 2, left). Next, we transformed both matrices into simpler two-dimensional forms (see Fig. 2, right) and normalized them with their corresponding standard deviations. In each of these 2-D matrices, each row represents the temperature information of any given day, and each column shows the evolution of a specific Landsat pixel over the last four decades. At this step, we employed the Singular Value Decomposition (SVD) method to decompose the dataset. SVD can reduce a sizeable multivariate dataset to a smaller one that still contains a significant fraction of the variability present in the original data (Brand, 2002; Wall et al., 2003). SVD decomposes the data matrix into three matrices:

$$M = USV^T \tag{5}$$

Here, the left vectors (columns of $\mathbf{U}$), singular values ($\mathbf{S}$), and right vectors (columns of $\mathbf{V}$) provide essential information about different modes of SST record. The singular value represents the strength of each mode. The left vector, at the same position as to operate on that singular value, illustrates the temporal oscillations of the modes. The matching right vector reveals its spatial pattern. In our analysis, we adopted the terminology of Paden et al. (1991) to designate EOFs magnitude as "covariance" because $M^T M$ is the covariance matrix whose eigenvalues are the singular values squared (Fox-Kemper, 2004). The computation of the covariance is expressed as $\sum_{j=1}^{m} S_j^2 / \sum_{i=1}^{n} S_i^2$, where j runs over the m modes of interest, and i runs over the n total number of modes (Fox-Kemper, 2004).

It is important to note that we excluded Landsat 5 satellite scenes from the pattern analysis to prevent any potential distortion (i.e., it skews all EOF time series to the left). Thus, the updated dataset contained only Landsat 7 and 8 scenes from 1999 to 2022, which resulted in a reduced number of scenes (453 scenes instead of the original 764). We want to emphasize that the EOFs themselves lack direct physical significance; they serve as a statistical orthogonal decomposition of the data matrix. Researchers must carefully interpret the results and establish correlations between EOFs and known physical forcings to avoid over-interpreting the findings.

4.4 Detrending and Isolation of the Climate Change Signal

We identified a local trend at every spatial location over the length of each record in both Landsat and buoy temperature. We calculated the trend using a least-squares regression similar to the one described above in the bias correction Section 4.1. However, here, we used the linear fit to estimate the deseasoned annual mean temperature at each grid point. First, we worked out the mean and trend coefficients by least squares from individual grid points to produce the detrended Landsat temperature. This fitting process follows the polynomial plus annual cycle equation:

$$SST(x,t) = b_s(x)\sin\left(\frac{2\pi t}{365.2425\,\mathrm{day}}\right) + b_c(x)\cos\left(\frac{2\pi t}{365.2425\,\mathrm{day}}\right) + c_0(x) + c_1(x)t + \xi(x,t) \tag{6}$$

Considering both spatial and temporal dependency of the SST in the bays, equation (6) can be written as

$$SST(x,t) = b_c(x)\cos(\Omega t) + b_s(x)\sin(\Omega t) + c_0(x) + c_1(x)t + \xi(x,t) \tag{7}$$

In both equations, c_0, c_1 are the mean and trend coefficients to be determined, b_s, b_c are the seasonal cycle coefficients, and $SST(x,t)$ is the grid point temperature as a function of space and time. We determined the annual cycle coefficients with the Fourier transform of the annual band (hence, $\Omega = \frac{2\pi}{365.2425\,\mathrm{d}}$). Since the seasonal sampling was uneven, we applied the Lomb-Scargle method (ref. to section 4.5) for this frequency band. We tested the robustness of the Fourier annual cycle by building a climatology instead of monthwise mean data and found similar results. Individual grid points then had their mean, trend, and annual cycle removed to produce the detrended, deseasonalized Landsat temperature record ($\xi(x,t)$). Next, we computed the uncertainty linked to each year by taking into account one standard deviation of the average temperature readings across all grid points for that particular year. Both spatial and temporal uncertainties are encompassed in the last term of equation (8), which is a space- and time-average of equation (7).

$$\langle \mathrm{SST} \rangle = \langle c_0 \rangle \tag{8}$$

We assumed that the linear trend is implemented in such a way that it does not contribute to the mean over the time window under consideration. Although the other terms in equation (6) vanish in the estimate, their uncertainty does contribute to the uncertainty in equation (8),

$$\langle \mathrm{SST}^2 \rangle - \langle \mathrm{SST} \rangle^2 = \langle \xi(x,t)^2 \rangle = \frac{\langle \sigma_x^2 \rangle}{N_x} + \frac{\langle \sigma_t^2 \rangle}{N_t}. \tag{9}$$

where σ_x, σ_t are the standard deviations of $\xi(x,t)$ in space and time and N_x, N_t are the number of degrees of freedom in space and time averaged over so that the ratios in (9) are the standard error of the mean in space and time. It is assumed that for this purpose, most of the uncertainty in c_0 results from sampling of variability in $\xi(x,t)$ rather than from misestimation of the linear and annual coefficients (b_s, b_c, c_1).

Equation (9) pertains to the inherent uncertainties in sampling, both in terms of space and time, arising from the shifts in climate conditions over the past four decades in the bay. To address spatial uncertainty, we initially created a composite of 39 image sets, each containing the deseasonalized average temperature data for a particular year. These pixel-wise averages were computed from all images collected in that year. Then, we applied bootstrapping to this collection of 39-year averages to compute the standard error for averages across the entire grid using 1000 samples for each step of the calculation for both bays. This approach of directly estimating the standard error rather than using the spatial standard deviation precludes the need to know the number of degrees of freedom N_x. As for the temporal sampling uncertainty, we measured the standard deviation (σ_t) of temperature measurements specific to each year. Then, we divided this value by the number of scenes (N_t) captured that year, i.e., assuming the different scenes are uncorrelated and independent. This number varied; for instance, eight images were collected in 1984 and six in 1985. The resultant temporal $\left(\frac{\sigma_t}{\sqrt{N_t}}\right)$ and spatial $\left(\frac{\sigma_x}{\sqrt{N_x}}\right)$ standard error uncertainties are visually illustrated in Fig. 4 to explain the annual and inter-annual temperature evaluation in section 5.2.

We employed the MATLAB 'detrend' function to eliminate the local trend from the buoy temperature record, which is similar to a least squares approach. We found negligible differences between this technique of detrending compared to the previous method described in equation (6) to determine c_0, c_1. As a case study, we applied both detrending methods to the SST record at the buoy 13 location (41.4922°N, -71.419°E) from 2004 to 2015. The linear fit applied for detrending the Landsat pixels located at buoy 13 location indicated a yearly rise of 0.0662 ± 0.0014°C, while using the 'detrend' function yielded a growth of 0.0671±0.0018°C. Buoy 13 records temperatures across all seasons, making it a suitable candidate for this analysis. Other buoys were deployed only during some seasons. We required the annual fit within equation (6) to arrive at a mean temperature that did not alias the variability from the seasons of deployment into the mean temperature.

4.5 Applying the Lomb-Scargle Method for Power Spectra

The Lomb-Scargle technique detects periodic signals (i.e., Fourier transforms) in time series data that may be unevenly sampled or have measurement errors. We used this method to isolate the tide-synchronous patterns within the temperature and surface elevation signals and to identify other underlying periodic signals in both buoy and Landsat records. Typically, the buoys log data at 15-minute intervals, but the recording is not uninterrupted, with some measurements taken out during the winter season. The Landsat records are also not evenly sampled because the removed scenes failed the cloud coverage threshold. Thus, a Fourier transform method that is robust to uneven sampling is needed.

The detrended signals, as described in section 4.4, satisfy the conditions required for the Lomb-Scargle technique; they are time-ordered, stationary, and periodic (Bretthorst, 2001; Glynn et al., 2006; VanderPlas, 2018). Additionally, both Landsat and buoy records contain enough data points to accurately extract the signal period and amplitude of the dominant frequency from the temperature signals. The equation for our analyses can be written as:

$$P(f) = \frac{1}{2\sigma^2}\frac{\left[\sum_{i=1}^{N} T_i \cos(\omega(t_i-\tau))\right]^2}{\sum_{i=1}^{N}\cos^2(\omega(t_i-\tau))} + \frac{1}{2\sigma^2}\frac{\left[\sum_{i=1}^{N} T_i \sin(\omega(t_i-\tau))\right]^2}{\sum_{i=1}^{N}\sin^2(\omega(t_i-\tau))} \tag{10}$$

Here, $P(f)$ is the power spectral density at frequency f, N is the number of SST counts in the time series, T_i is the temperature at any given time t_i, $\omega = 2\pi f$, σ^2 is the variance of the temperature values, and τ is the time offset or phase defined by:

$$\tau = \frac{\sum_{i=1}^{N}\sin(2\omega t_i)}{\sum_{i=1}^{N}\cos(2\omega t_i)}$$

Specifically, for the buoy record, we employed Welch's power spectral density estimate technique (Attivissimo et al., 2000) on the seasons and tides. The main advantage of Welch's

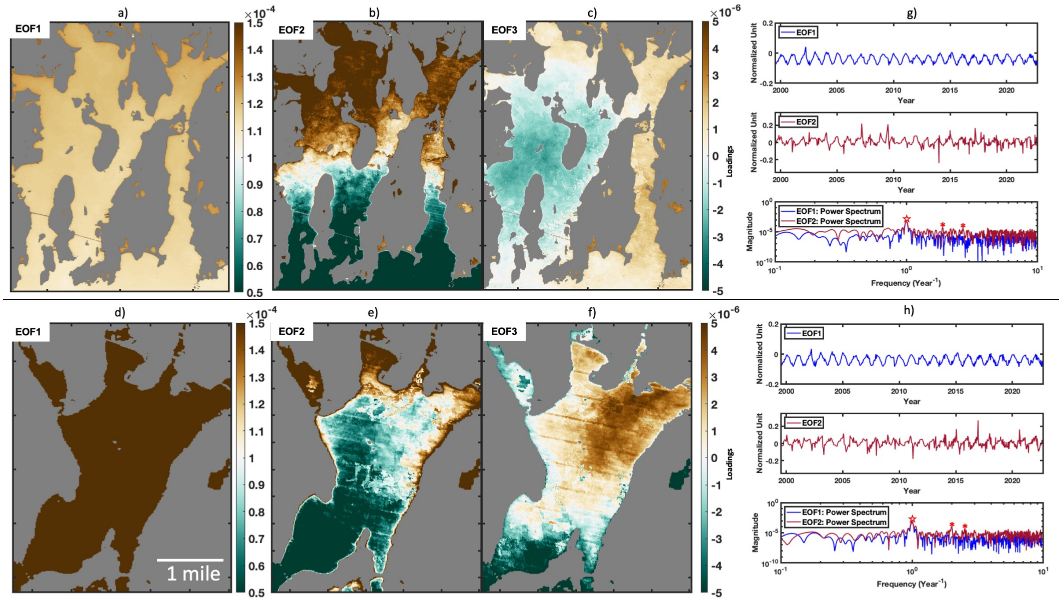

Figure 3. Spatial and temporal EOFs of Narragansett Bay and Mt. Hope Bay. a-f) The first three modes of the spatial EOFs of the bays. The upper panels of g and h represent the time series (eigenvectors) of the first two modes. The peaks in the power spectrum for EOF1 and EOF2 show that the seasonal cycle dominates both modes.

method is it splits a signal into overlapping segments and uses a window function to estimate the power spectral density estimation accurately.

5 Results and Discussion

5.1 Dominant Patterns

Empirical Orthogonal Functions (EOFs, Section 4.3) were utilized to analyze a time series of Landsat images for Narragansett Bay and Mt. Hope Bay, aiming to identify the dominant patterns of sea surface temperature variability.

5.1.1 Narragansett Bay

The first covariance mode (Fig. 3, panel a) accounts for 67.2% of the variability in the sea surface temperature of Narragansett Bay. The spatial amplitudes (loadings) show a positive and nearly consistent pattern across the entire map except in the open ocean, where the amplitudes are about 20% lower. The time series initiates from 7 July 1999 and is characterized by positive loadings ($\sim 10^{-4}$) in every pixel across the bay. The first mode of the spatial pattern indicates the entire temperature of the bay rises and falls simultaneously. In reality, this mode represents the seasonal cycle in SST. The EOF1 time series (eigenvector) reflects a standard sinusoidal temperature fluctuation (top row, panel g). Our interpretation is further solidified when we observe the prominent peak at 12 months (annual cycle) in the power spectrum of the EOF1 signal (bottom row, panel g).

The EOF2 mode represents 11.5% of the total variance (34.6% of the nonseasonal variance). The spatial patterns (Fig. 3, panel b) show greater positive loadings ($\sim 10^{-5}$) for the shallower waters in the northern segment of the bay. In contrast, the spatial amplitudes in the middle (at 40.60°N) portion of the Bay remain close to zero. Finally, the loadings become slightly more negative ($\sim 10^{-5}$) as we move towards the deeper ocean. This observation indicates that the shallower areas show greater variability compared to the rest of the bay. The upper bay is more sensitive to sudden heating and cooling because the continental land masses cool down and heat up faster than the ocean. The eigenvectors (middle row, panel g) for the EOF2 mode reveal pronounced peaks mainly during the spring and lower values during the falls. The power spectrum for EOF2 (bottom row, panel h) peaks at a frequency of 12 months, along with smaller peaks at 20 and 28 months. Our interpretation is the time series of the second mode reflects an additional underlying seasonal cycle. This cycle primarily indicates that shallow rivers and bay waters heat up (spring heating) or cool down (fall cooling) before the deeper offshore waters do.

Since the first two EOF modes explain up to almost 80% of the total temperature variabilities, we were primarily interested in the spatial and temporal pattern of these two modes. Regardless, we briefly commented on the spatial characteristics of the third mode (Fig. 3, panel c). EOF3 mode explains 8.2% of the overall variability and 24.4% of the non-seasonal variance. The east flank of the bay shows a stream of water with higher amplitudes running towards the ocean. We suspect this greater temperature sensitivity is caused by the differences in flow distribution between the two main channels (East Passage and Sakonnet River). The freshwater movement in the east passage of the bay is attributed to the limited estuarine outflow from the Providence River, residual circulation, and circulated vertical mixing induced by tidal forces over shallow bathymetry. Conversely, the eastern flank of Newport undergoes stronger freshwater discharges from the Taunton and Sakonnet Rivers (MacDonald, 2006), with a higher mean flow rate of $27\,\mathrm{m^3\,s^{-1}}$ and $55\,\mathrm{m^3\,s^{-1}}$, respectively.

5.1.2 Mt. Hope Bay

As Mt. Hope Bay is a part of Narragansett Bay, we expect similar behavior across different EOF modes. The EOF1 and EOF2 (both spatial and temporal) feature similar estuarine SST patterns as the rest of the bay (Fig. 3, panel d, e). The first mode represents the dominant radiative cycle and explains up to 80% of the total variabilities in the dataset. Given the location of Mt. Hope Bay in the upper bay, it is expected to be more responsive to seasonal temperature changes. EOF2 captures SST variation (7%) due to the depth-variability and freshwater input from the Taunton River. The power spectrum of the eigenvectors reveals peaks corresponding to the annual cycle in mode one and additional peaks at 12, 20, and 28 months in mode two, indicating physical changes are nearly persistent throughout the bay. The EOF3 (Fig. 3, panel f) endures the long-lasting effect of thermal effluents originating from the Brayton Point Power Station, as discussed in work by Benoit and Fox-Kemper (2021).

5.2 Annual and Interannual Cycle with Trends

The most significant SST variation in the bay occurs annually. This 12-month cycle masks high-frequency climatic trends (e.g., tides and waves) but reveals other important climatological insights, like warming trends. Narragansett Bay is warming up. The average annual temperature record from 1984 to 2022 strongly points toward a warming trend of 0.061 ± 0.024°C yr^{-1} for Narragansett Bay and 0.041 ± 0.018°C yr^{-1} for Mt. Hope Bay (see Fig. 4, panel a). The highest-ever spatial average of yearly mean sea surface temperature occurred in 2013, reaching close to 16°C, while the lowest was observed in 1992 at about 8.25°C. It is important to note that the temperature record from the Landsat 5 satellite between 1984 and 1999 shows greater inconsistencies due to scan-correlated level-shift noise (Welch et al., 1985) and low-frequency coherent noise (Metzler & Malila, 1985). However, with technological progression, the later releases (i.e., Landsat 7 and 8) recorded the temperature trend with more spatial and temporal precision after 1999.

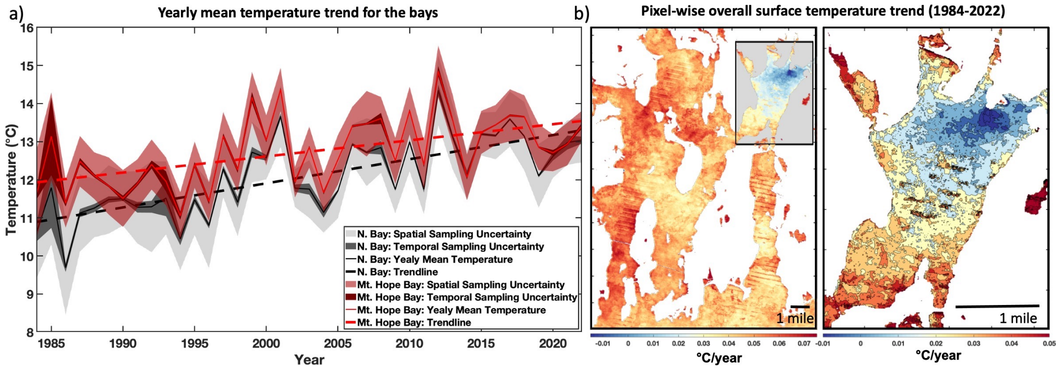

Figure 4. a) Annual sea surface temperature trend of the bays. Each data point shows the annual average temperature c_0 over the area and one standard deviation uncertainty. b) A linear fit after removing the seasonal cycle was used to calculate the trend (c_1 given in °C yr^{-1}) of the temperature change for each pixel over 39 years.

Interestingly, the warming trend of the bay is inconsistent throughout. Fig. 4, panel b shows the spatial map of the SST trends. The color of each pixel indicates the trend in the degree of temperature rise or decline over the past 39 years. We can identify a few regions around Prudence Island, Jamestown, and Patience Island as 'hot spots' because they are experiencing the highest ($\sim$ 0.7°C per decade) increase. There is no natural cooling except in the former location of Brayton Point Power Station, which was completely shut down after 2011 (Benoit & Fox-Kemper, 2021).

5.3 Seasonal Distribution of SST

The 39-year-long SST record provides better clarity of the temperature distribution across different months and seasons in the Bay. We reported the months of winter, spring, summer, and fall seasons as D-J-F, M-A-M, J-J-A, and S-O-N, respectively. The seasonal cycle is the most influential driver of the temperature distribution and variabilities in Narragansett Bay. Additionally, the unique location of the bay as an estuary, neither subtropical nor purely marine, may introduce additional factors to play minor roles—for example, the vertical mixing of fresh and brackish water and localized ambient air temperature (Chen & Harr, 1993; Deser et al., 2010; Alexander, 2010).

The spatial variability of the seasonal cycle reveals distinct SST patterns across different water bodies in the bay (Fig. 5). Due to the global amplification of shallow water temperature (Oczkowski et al., 2015; Piccioni et al., 2021), we identified a clear signature of latitudinal temperature distribution in the bay (Fig. 5, panels a-d). Isolated and shallow areas feature pronounced temperature variations (-1 to 31°C) compared to the deeper, well-connected embayments (1 to 25°C) and the ocean (5 to 17°C). Since the northern segment of the estuary is fresher, has a reduced heat capacity, and is more sensitive to any sudden change in air and river temperatures, from here, we will refer to them as the upper (41.60°N to 41.75°N) and the lower (41.60°N to 41.45°N) bays.

The intensity of seasonal cooling and heating in the bay varies throughout the year, with the ocean temperature showing a delayed response compared to the estuarine temperature. A closer look at the SST map reveals that the maximum cooling occurs in January for the upper bay, while the lower bay experiences this in late February (Fig. 5, panel a). On the other hand, the maximum heating occurs around mid-August in the upper bay, followed by the shelf approximately one month later (Fig. 5, panel c). The maximum temperature difference between the upper bay and the lower bay can be as much

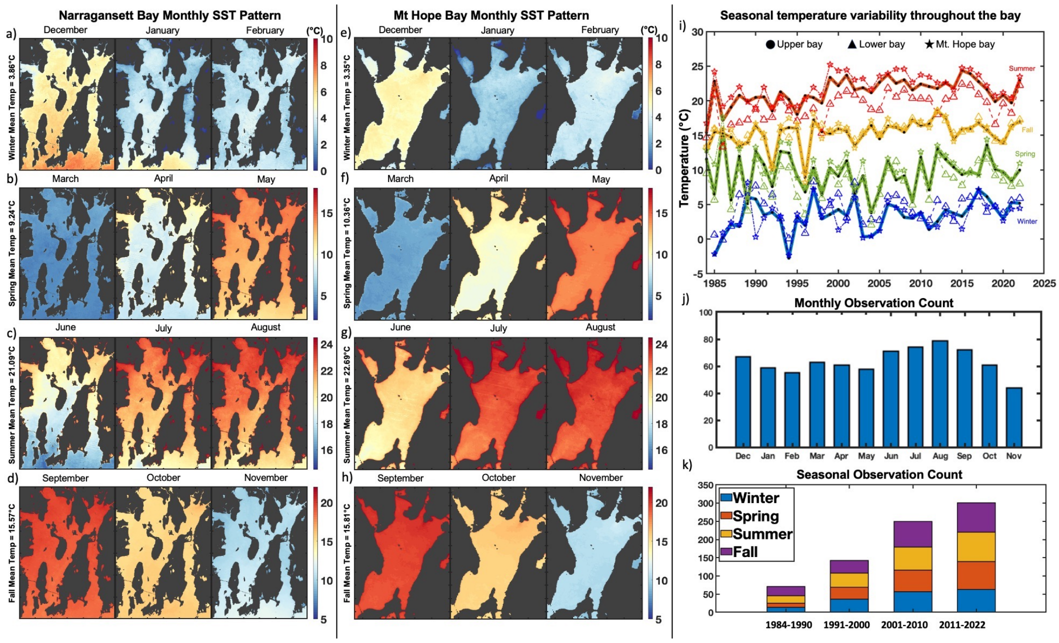

Figure 5. a-h) Seasonal and monthly average temperature variabilities in the bays. i) Temperature variability across different seasons in the upper and lower bays, and j, k) Observation counts per month and season, respectively, over 39 years.

as 4.25°C in August. This difference can further increase up to 6.75°C in December. Mt. Hope Bay is characterized by its small size (approximately 13 mi^2 or 36 km^2) and an average depth of 18.7 feet. Therefore, we do not see any significant spatial variability in the annual SST cycle (Fig. 5, panels e to h). Over the last four decades, we observed the average seasonal extremes (difference in SST between summer and winter) to be 19.65°C in Narragansett Bay and 21.08°C in Mt. Hope Bay. The springs (9.24°C) are generally colder than the falls (15.57°C); refer to Fig 5, panel i. The observation counts are almost the same throughout all seasons, and there has been a steady increase in the number of observations since the release of Landsat 7 in 1999 (Fig. 5, panels j and k).

5.4 Decadal Variability

We analyzed the evolution of the seasonal temperature shifts in Narragansett Bay (Fig. 6). The process is as follows: we created the maps of decadal mean temperatures for each season (see Fig. 6, panels a-h). As we move forward to the positive time axis (to the right) of each map, we can see how individual seasons are evolving. Here, we are presenting an example to explain the statistical analysis: we captured 57 images during the winter season from 2001-2010. At first, we averaged the temperatures of all 57 scenes and combined them into a single composite. Then, we calculated the standard deviation of the composite image. This tells us how the overall temperature of each grid varies spatially during the winters of 2001-2010. Then, we divided the mean standard deviation by the square root of the number of scenes to calculate the standard error of the mean. Intuitively, the standard error is the standard deviation of the sampling distribution. Mathematically, this process can be expressed as:

$$\text{Standard Error Uncertainty} = \frac{1}{\sqrt{N}} \cdot \frac{1}{M} \sum_{i=1}^{M} \sum_{j=1}^{N} \text{Std}(T_{ij}) \tag{11}$$

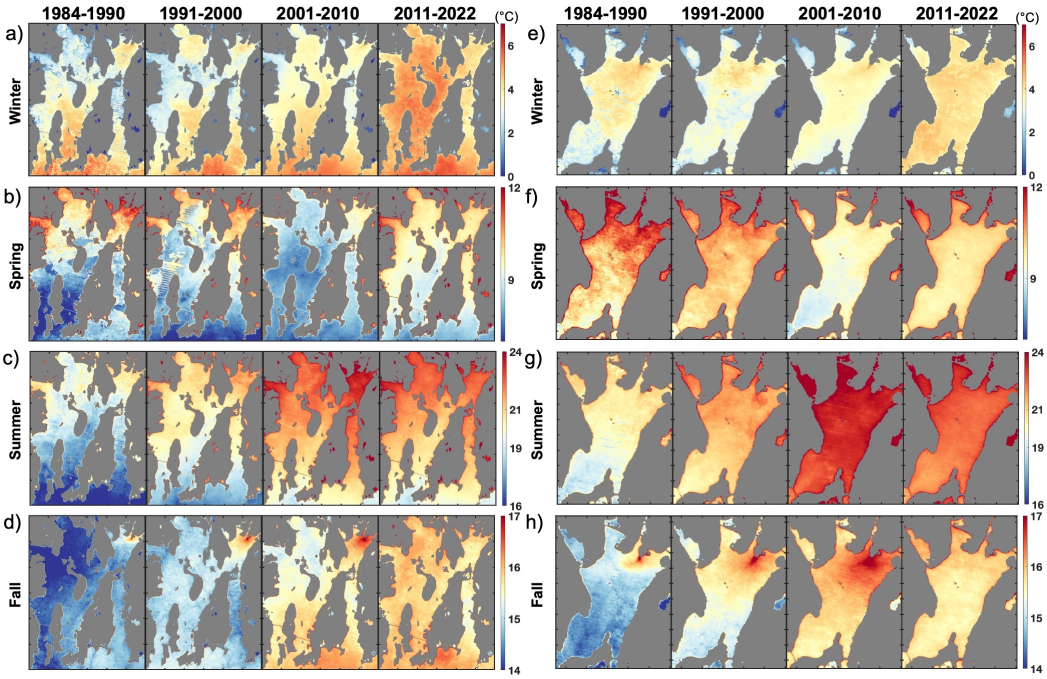

Figure 6. Approximately decadal averages of the annual averages of temperature in the bays.

In equation (11), N is the total number of scenes (57 in this case). M is the total number of pixels in each image. Std(T_{ij}) calculates the standard deviation of the temperature values at pixel (i, j) across the set of 57 images. We presented the quantities denoting the sample size and the corresponding sampling uncertainty of every season in the decadal time scale in Table 3.

Narragansett Bay, especially in the last two decades, underwent considerable changes due to global climate warming and anthropogenic influences (Fig. 6, panel a-h). The winters are getting warmer rapidly. In contrast, we found a cooling trend in SST during spring from 1991 to 2010. However, the average spring temperature increased after 2011. The summer experienced the most significant warming over the past two decades, particularly between 2001 and 2010. This event coincided with some of the warmest summers recorded in the last four decades. The influence of thermal effluents from the Brayton Point Power Station is most noticeable in the average fall temperature maps, primarily attributable to the increased activity at the power station during this season. The thermal pollution imprints intensified until 2010. In later years, it abruptly diminished due to the complete cessation of the power station in 2011. Even without this anthropogenic source, the spatial trend indicates that the falls in the bay are getting much warmer since 2010 compared to two decades ago.

We can observe similar climatic shifts in the decadal SST variations of Mt Hope Bay (Fig. 6, panels e to h). 2001 to 2010 witnessed the coldest spring and the warmest summer recorded. The signature of the power station was particularly noticeable in the winter and fall seasons but disappeared after 2011. The distinction between the upper and lower parts of Mt. Hope Bay is not as pronounced when compared to the whole bay. This feature is likely due to the smaller size and consistent depth across its expanse. Still, we noticed significant temperature changes over the last 39 years near the shorelines, especially around the Kickemuit River shellfish management area (average water depths $\sim$ 6 m). Our observation points to the potential adverse effects of increasing SST on the local fisheries. Previous research has consistently shown that increased SST leads to el-

Table 3. One Standard Deviation Decadal Sampling Uncertainties in Narragansett Bay and Mt. Hope Bay

Seasons	Year Span	Sample Size	Sampling Uncertainty (°C)	
			Narragansett Bay	Mt. Hope Bay
Winter	1984-1990	14	0.4478	0.5208
	1991-2000	36	0.2800	0.3511
	2001-2010	57	0.3028	0.3384
	2011-2022	63	0.2626	0.3213
Spring	1984-1990	11	0.4648	0.5673
	1991-2000	33	0.3216	0.3857
	2001-2010	59	0.3074	0.3767
	2011-2022	76	0.2952	0.3275
Summer	1984-1990	20	0.5843	0.6272
	1991-2000	39	0.3251	0.3986
	2001-2010	63	0.3031	0.3518
	2011-2022	81	0.2589	0.3180
Fall	1984-1990	26	0.3358	0.4108
	1991-2000	34	0.3170	0.3938
	2001-2010	71	0.2719	0.3140
	2011-2022	81	0.2740	0.3264

evated CO_2 levels, low oxygen conditions, and amplified acidification. These collective effects can harm shellfish, impede their growth, compromise their immune responses, and impair their overall cultivation prospects (Heath et al., 2012; Cocco et al., 2013; Mackenzie et al., 2014; Cruz et al., 2015; Hernroth & Baden, 2018; Harrison et al., 2022).

5.5 Can we capture tidal SST anomalies from Landsat scenes?

Tides can profoundly govern the biological, physical, and morphological features of any tidally dominated estuaries (Wells, 1995; Nidzieko, 2010; Cheng et al., 2011; Dalrymple et al., 2012). Narragansett Bay is a tidally dominated estuary with a semi-diurnal M_2 tide system (Bowers & Brubaker, 2021), and much of its high-frequency oceanographic characteristics can be attributed to its tidal forcing (Spaulding & Swanson, 2008). While the Landsat record offers climatological insights into SST patterns, our primary focus in this section is to evaluate and measure the Landsat's accuracy in sampling SST changes during various tidal phases, including high tide, low tide, ebb tide, and flood tide. Due to the diurnal inequality (De Boer et al., 1989), the bay has a variety of tidal ranges. Therefore, when we look at the water level at any particular time over many days, we will notice variations in the amount of sea level elevation, exposed tidal flats, and inter-tidal areas. Landsats capture scenes at about the same time each visit due to its sun-synchronous orbit (Wulder et al., 2019). So, for the past 39 years, Landsat had overpassed the bay at various tide levels. As a result, our collection of satellite photos will show different tidal phases and the temperature of the bay at any given tide phase.

Given that the Landsat SST record has an average sampling rate of about 18.75 days in our dataset, the Nyquist frequency is 37.5 days. Therefore, the Fourier analysis of the Landsat record can not directly provide information at tidal frequencies. From Fig. 7, panels a and b, the power spectrum of the satellite SST signal shows peaks at the annual cycle (1 year). However, from Fig. 7, panels c and d, we notice that the high-frequency buoy SST record allows us to retrieve information at the diurnal cycle (1 day),

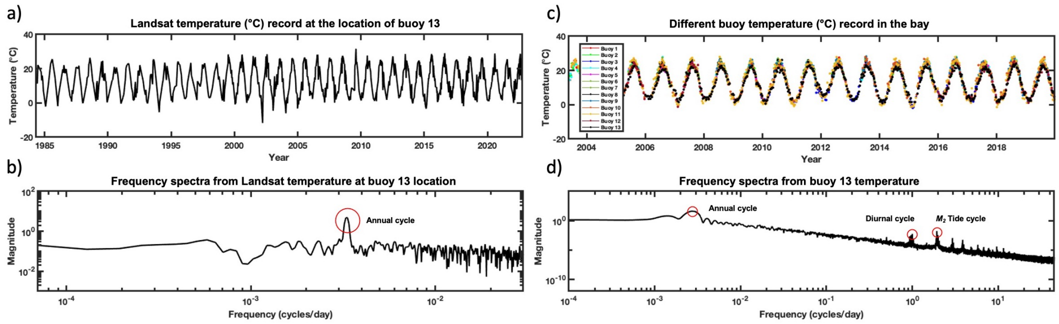

Figure 7. a-b) The frequency spectrum of the SST record shows that Landsat can capture the annual cycle but fails to resolve small-scale temporal SST pattern like M_2 tides that occurs every 12 hours. c-d) Buoy SST record can resolve this limitation. In both cases, we chose buoy 13 as an example.

M_2 tide cycles ($\sim$12 hours), and the annual cycle (1 year). The peak magnitude at $\sim$2 cycles day^{-1} implies that tide predominantly regulates the water temperature variability of the bay immediately after the seasonal cycle. The diurnal cycle is also important, but as Landsat is sun-synchronous, the approach we use for tides cannot be extended to this cycle.

To evaluate the tidal sampling from Landsat, we proposed a 'composite view' of tidal SST patterns by two distinct methodological approaches. The first approach, the Signal-to-Noise ratio (SNR) test, evaluates the ratio between the desired signal (representing the tidal SST variability) and its background noise (other variability). The second method is predicated on the notion that during inter-tidal phases, instantaneous water-level depth (H) and temperature (T) ought to be correlated. Most simply, if water from the ocean either advances inland or recedes to the sea with the tides, it will impact both instantaneous water level height and temperature. We named the second approach the HT method.

Since we are limited to particular buoy locations, we conducted this test in two distinct regions, near buoy 11 (41.6861°N, -71.4459°E) and buoy 13 (41.4922°N, -71.419°E). These buoys were strategically chosen as representatives of the upper and lower bay, respectively (See Fig. 1, panel a). As discussed in Section *5.6.1*, the upper and lower bay show different characteristics in SST variability, and other buoy locations tended to resemble one or the other of these locations.

For the Signal-to-Noise ratio test and the HT method, we leveraged the principle of "stationarity" and "simultaneity". Stationarity suggests that tidal fluctuations possess consistent duration and impact across the bay over an extended period of repeated tidal cycles (e.g., neglecting lower frequency tides and other variations). Simultaneity posits that despite the location of one of the stations in the southern part of the bay (refer to Fig. 1, panel a), the phase propagates sufficiently quickly into the bay that all stations are effectively at the same tide phase during a 60-minute SST sampling window or Landsat scene. Simultaneity was validated by comparing it to other tide gauges throughout the bay.

5.5.1 Signal-to-Noise ratio test

The signal-to-noise ratio (SNR) measures the clarity of a signal by distinguishing it from background noise. In our case, the desired signal is the SST anomalies caused explicitly by the tidal forcing. To perform the SNR test, we first synced the dates of Land-

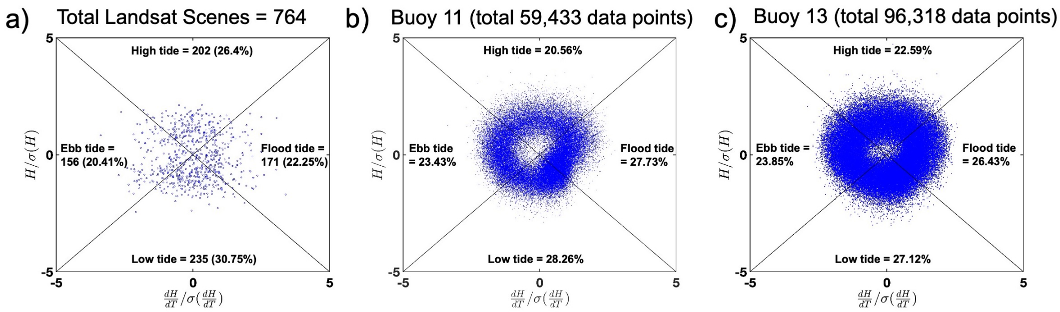

Figure 8. a-c) The tide-phase-shift diagram from the times where a) Landsat scenes are analyzed, b) Buoy 11 data is available, and c) Buoy 13 data is available.

sat images from 1984 to 2022 and the buoy record from 2004 to 2022 with the corresponding NOAA tide gauge station data. Then, we sorted the images into a composite of four tide phases based on a so-called 'tide phase shift' diagram. This diagram is divided into four sections, each of which is representative of one tide phase (see Fig. 8). In this diagram, the sea level elevation (H) and its time derivative ($\frac{dH}{dT}$) are normalized by their respective standard deviations.

The inter-tidal temperature of an estuary is primarily influenced by the sea surface temperature during high tides and by the air temperature during low tides (Scrosati et al., 2020). Landsat cannot track individual tidal phases due to its sampling frequency. However, the four sets of composites give a general overview of the spatial distribution of the SST anomalies during different tidal stages (see Fig. 9, panels a and b). To isolate the tidal SST variability from any contamination caused by the seasonal cycle and climate-driven warming, we deseasonalized and detrended each pixel in the image sets. We expect this filtering step will ensure the composites are mainly linked to the tides, and there will be no strong seasonal variations in tidal patterns (e.g., the tidal SST excursion in summer is similar to the tidal SST excursion in winter). The adjusted Landsat pixels of the bay now show cooler temperatures, typically ranging from -2°C to 2°C, because of the removal of the monthly mean temperature, radiative cycle, and the warming trend.

We evaluated the strength of each Landsat composite to capture the imprint of tidal SST variations (signal) against the remaining variations (noise) that were coherent with diurnal cycles, winds, river runoff, and other local factors. Assuming a Gaussian distribution, we calculated a mean temperature (μ) for each pixel and standard deviation (σ) of the means for each composite over the entire bay. The standard error of the mean is $\frac{\sigma}{\sqrt{N}}$. Here, N corresponds to the number of observations, which is 235, 171, 202, and 156 for low, flood, high, and ebb tides, respectively. We followed the approach of Johnson (2006) to describe the SNR to be the ratio of the squared mean temperature (μ^2) of any given pixel to the standard error $\frac{\sigma}{\sqrt{N}}$ in decibels. We defined the statistical significance to be a signal-to-noise ratio of 1.645. This ratio sets the threshold for a 95% confidence level by a one-sided Student's t-test. Any pixel that could not meet this threshold was marked in yellow (see Fig. 9, panels c and d).

The results from the SNR spatial maps explain the outcomes of the typical tidal interaction between deep ocean water and offshore water. The signal clarity is compromised during the low and ebb tides in Narragansett Bay and the flood and ebb tides in Mt. Hope Bay. Our interpretation is that during the flood and high tides, heat exchange through vertical mixing between the relatively colder ocean and the warmer offshore and river waters can lead to greater short-term sea surface temperature variability (Garrett

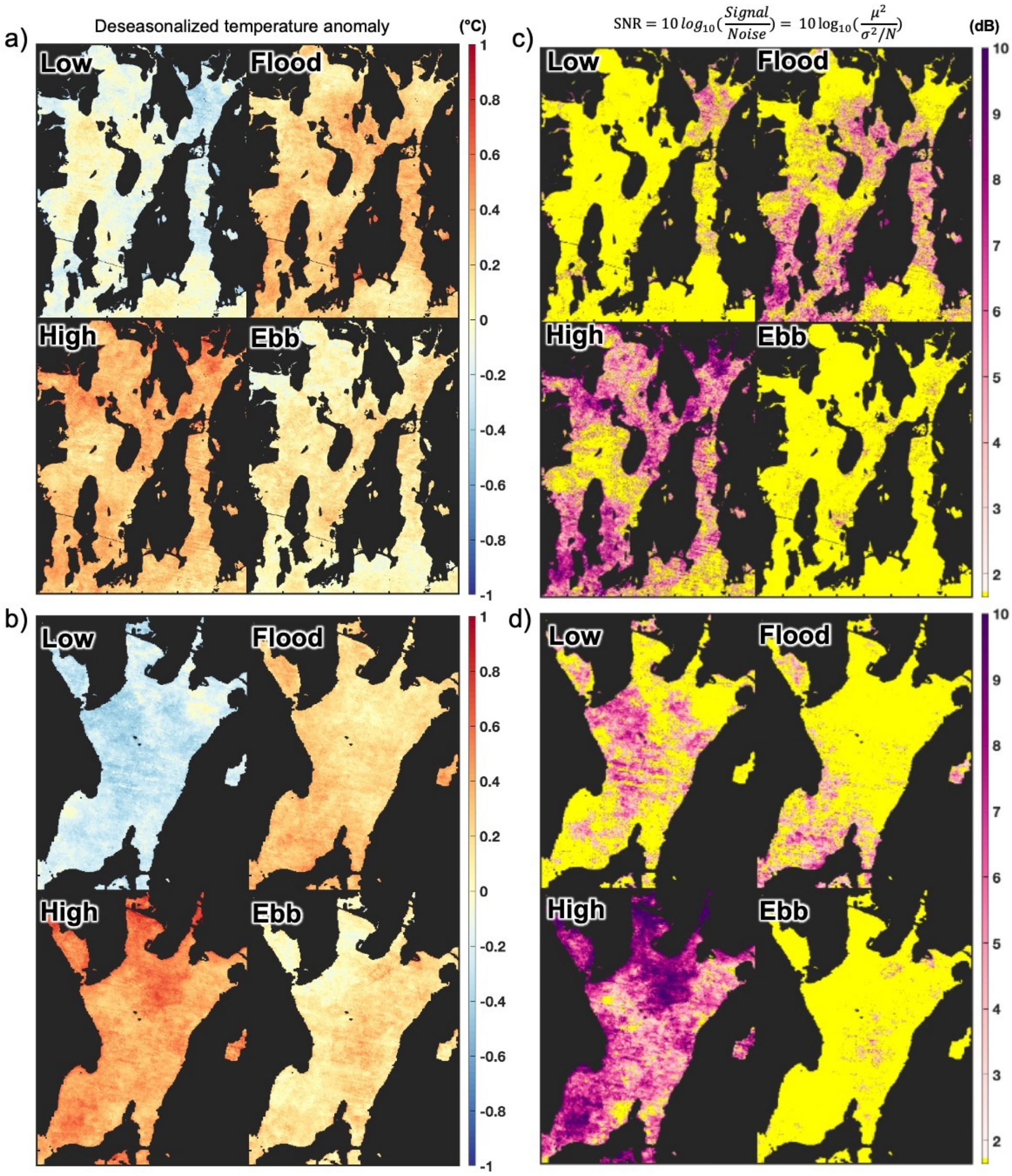

Figure 9. a-b) Temperature anomalies of Landsat composites in different phases of tides after the seasons and warming trends are removed. c-d) The pixels where the squared mean temperature is greater than the uncertainty are shown in pink. Any pixel that is identified with SNR<1.645 (significant noise) is denoted in yellow. The intensity of the signal is presented in panels c and d in decibel units.

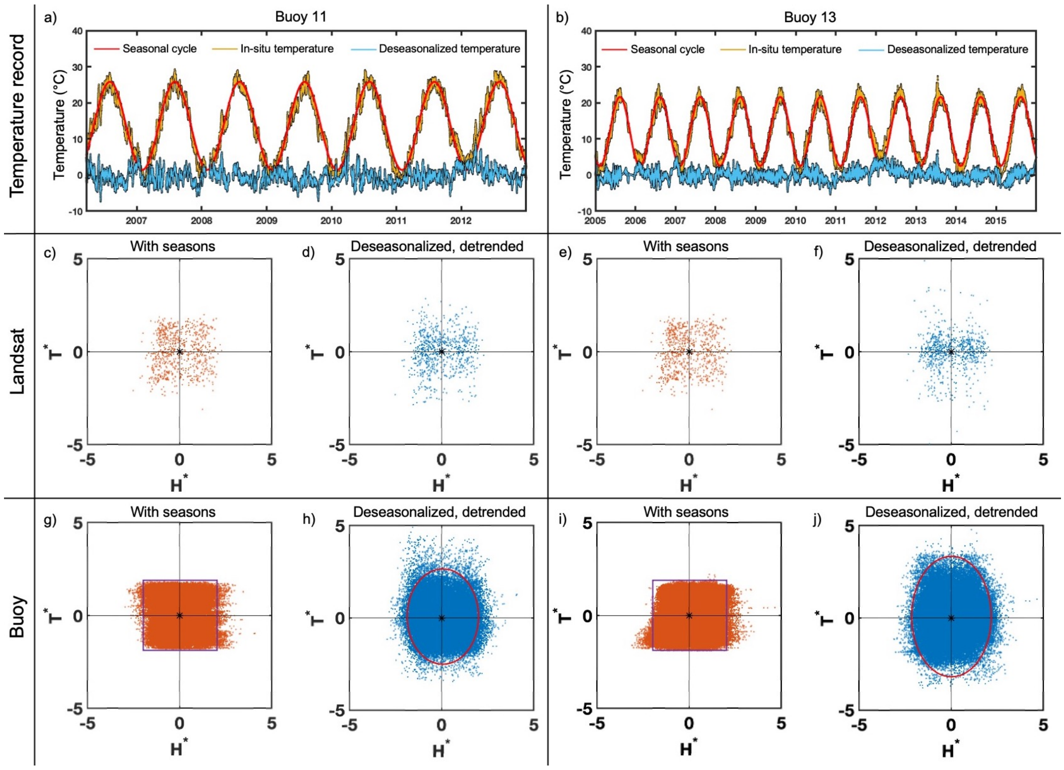

Figure 10. a-b) Representation of SST fluctuations due to seasonal cycle and tidal forcing in buoy 11 and 13 locations. c-j) Temperature variability against its instantaneous sea level elevation, with and without seasonal influence. Panels c to f represent data from Landsat grids where the buoys are located, while panels g-l show results directly from buoy readings.

et al., 1978; Simpson et al., 1994). Hence, this tidal mixing forces the bay to undergo episodic cooling or warming (depending on the season). Since we defined this temperature variability as the 'signal' in our SNR test, we observed the Landsat composites to partially capture this signal (Fig. 9, panels c). In Mt. Hope Bay, during the high tides, ocean water approaches through a narrow passage of the Sakonnet River. This restriction can cause internal tidal asymmetry (Jay & Musiak, 1996) and greater temperature variability, which is captured in the Landsat composites as well (Fig. 9, panels d).

5.5.2 HT method

In this section, our objective is to explain Landsat's capacity to reveal the underlying tidal temperature variability without arbitrary distinctions by binning it into tidal phases. We developed the HT method based on the notion that the influx of cold ocean water influences the temperature within the estuary regularly and periodically. The pattern of this influx predicts a correlation between an instantaneous sea level elevation (H) and estuary temperature (T). Given the limited temporal resolution of Landsat data, capturing daily changes becomes challenging. Therefore, in examining correlations, it is easy to contrast Landsat against buoy temperature records of the relationship between H and T. Another advantage of this model is we can more easily conduct this test using seasonal and nonseasonal datasets to assess the significance of seasonal influences. We obtained consistent temperature measurements from buoy 11 between 2006 and 2013 and buoy 13 from 2005 to 2016 (see Fig. 10, panels a and b). Both temperature records are extensive enough to be adequate for the application of this method.

The HT diagram illustrates any covariance between sea level elevation and estuary temperature (Fig. 10, panels c-j). This diagram is similar to the 'tide-phase-shift' diagram (ref. to Fig. 8). However, this time, we plotted temperature (T) as the distance against the corresponding sea level height (H). Unlike making composites based on Fig. 8, it is not necessary to discretize the tidal phases in this figure–continuous values are allowed. If the temperature does not vary coherently with sea level elevation, there is no covariance between H and T; hence, $\overline{H(t) \cdot T(t)} = 0$. If a covariance exists, then in the HT diagram, some phases will register as warmer (farther from the origin) and others as cooler (closer to the origin). In this case, we can expect to see the plots form an ellipse or an oblong circle. We normalized the parameters using their respective z-score values for better interpretability and comparability, e.g., H^* and T^*, where

$$H^*(t) = \frac{H(t) - \mu_{H(t)}}{\sigma_{H(t)}}$$

and

$$T^*(t) = \frac{T(t) - \mu_{T(t)}}{\sigma_{T(t)}}$$

The HT diagrams with seasons show that both Landsat and buoy temperatures are equally distributed and do not correspond to the tidal phases. As the seasonal variability is dominant and uncorrelated with the tidal forcing, it masks any H-T relationship (Fig. 10, panels c, e, g, and i). In this case, the seasons act as 'noise' rather than a signal. The distribution of T^* appears almost quadrilateral because regardless of the sea level height, temperatures rise and fall in line with the seasonal cycles. As a result, there are nearly equal data points on both sides along the $H^* = 0$ axis line. This makes the HT diagram appear 'symmetric', and we can not draw any meaningful correlation between H^* and T^*.

The deseasonalized temperature record changes the shape of the distribution, suggesting that $\overline{H^*(t) \cdot T^*(t)} \neq 0$. The distribution now appears more elliptical and reveals a link between the sea level depth and the corresponding water temperature. Since we do not have sufficient Landsat scenes, the HT diagram results in a scatter plot without any definite geometrical shape (panels d and f). Thus, the Landsat is limited in capturing connections between SST changes caused by tides in the bay. In contrast, the scattered plots from buoys 11 and 13 closely resemble an elliptical shape and prove the existence of an underlying relationship between H^* and T^*. In summary, it is challenging to detect sea level correlation with SST variability using low sampling rates and instrumental inaccuracy. Only with heavy averaging over multi-year composites, as in the previous section, Landsat might detect signals in some tide phases.

The HT diagram provides a visual representation of the relationship between the sea level elevation and the instantaneous temperature, but it lacks quantitative analysis. We constructed standard histograms of the distribution resulting from the multiplication of H(t) and T(t). In this step, we normalized both H and T with their standard deviation instead of using H^* or T^* for scale independence and better interpretability of the result by keeping the mean value close to the original data. The $\frac{H(t)}{\sigma_{H(t)}} \cdot \frac{T(t)}{\sigma_{T(t)}}$ histograms display the interference of the seasons in the buoy locations (Fig. 11, panels a-d). Eliminating seasonal factors decreases both fluctuations and background disturbances, as is evident in the x-axis spreads in panels b and d. Both Landsat and buoy exhibit a roughly Gaussian distribution when seasons are removed. Still, they are indistinguishable from zero–i.e., there is no detected typical correlation for each sample.

It is plausible that taking an ensemble could highlight a representative value, so we examine the bootstrap histograms for the means (Fig. 10, panels e-h). The bootstrapped mean histograms show a Gaussian distribution with and without seasons. The season-inclusive bootstrapped distributions disagree in both mean and spread (panels e and g).

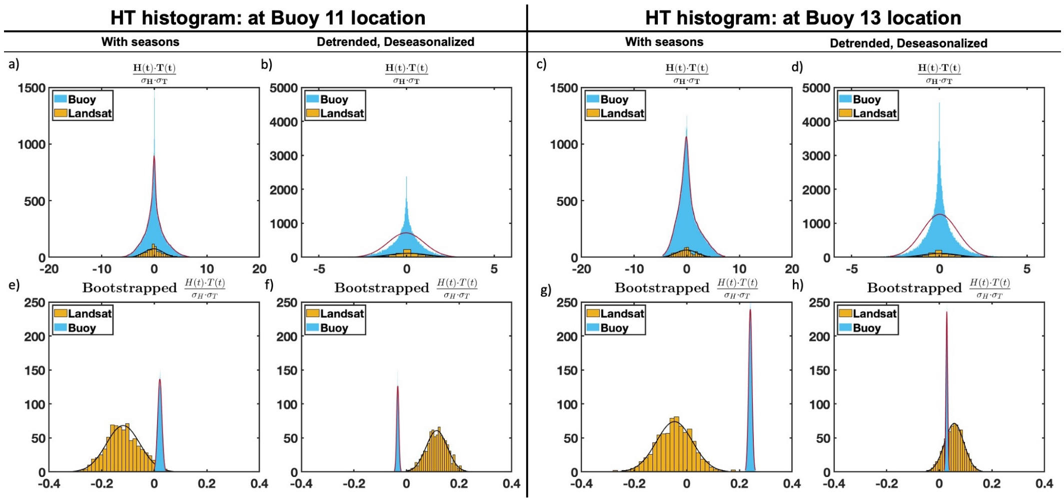

Figure 11. a-d) The statistics of samples of $H(t) \cdot T(t)$. e-h) bootstrap histograms estimating their mean. Seasons and trends must be removed from the Landsat temperature in order to have Landsat and buoy distributions agree on the mean value (as shown by bootstrap histograms), and even then, the Landsat histograms are wider (more instrumental error) than the buoy temperatures.

Thus, there is no consistency between the buoy and Landsat mean correlations in seasonal SST data. Once the seasons are removed, the bootstrapped distributions align more closely and suggest a mean value with lower variation (panels f and h). There are three key findings from these histograms. First, the use of standard error in the previous section was appropriate but might only yield a consistent signal between the buoy and Landsat records after the removal of the seasons and trends. Secondly, the tidal patterns are not detectable until the seasons are removed due to the strong seasonal variability and the intermittent sampling of it by the Landsat. Thirdly, the estuary variability is greater than that of ocean variability. Buoy 11 is located in the upper bay, close to the coastlines. We observed a 50.3% broader spread in its mean histogram before we removed the season (panels e-f). For buoy 13, which is located near the ocean, the spread was 45.1% broader before the removal of the seasons (panels g-h), which indicates more consistent and limited variability throughout the year.

6 Conclusion

The techniques and findings presented in this study have significant implications for coastal oceanography. By integrating data from on-site sensors with satellite observations for calibration, we improved the estimation of sea surface temperature at different spatial scales near the coast. This approach overcomes the limitations of limited spatial-resolution data from in-situ sensors, which fail to capture the spatial variability in the bay. Through the application of the EOF algorithm, we successfully identified and quantified sea surface temperature patterns in both Landsat and in-situ buoy temperature records. This pattern recognition technique also indicated the dominant components that are influencing the SST distributions, like the seasonal cycle and estuary bathymetry. From the spatial decadal variability of SST, we clearly observed that global warming is affecting the bay.

Our analysis demonstrates that the tidal signal is the next-most important determinant of SST in the bay after seasonality. This finding was only possible due to robust sampling and instrumental precision, given the presence of noise and aliasing effects. We presented two different methods to quantify the extent to which we can use Landsat satellite to capture the tidal SST anomalies. The methods offer a path to studying tidal patterns in coastal temperature records and have implications for future coastal oceanography and estuarine ecology studies. By leveraging the composites of Landsat scenes in different tidal phases, we have analyzed the tidal characteristics of Narragansett Bay. The result can serve as a model for other tidally dominated estuaries (e.g., Fitzroy River estuary, Australia; Clear Water Bay, Hong Kong; Puget Sound, Seattle) that lack access to in-situ buoys but have alternative measurements, such as tide gauge and ship observations or tide gauge and drone observations.

7 Acknowledgements

We thank Lorenzo Davidson and Frank E. Fisher for their assistance with data collection and preparation. We acknowledge the conversations with Dr. Daniel M. Watkins regarding the physical dynamics of Narragansett Bay and helpful references. AA, BFK, and DW were supported by NSF OIA 1655221, and AA was also supported by a Rhode Island Science and Technology Advisory Council award. The buoy-calibrated Landsat record for Narragansett Bay is available at `https://riddc.brown.edu`. Patterns and analysis code are available at `https://repository.library.brown.edu` under `https://doi.org/10.26300/pqpe-fe67`.

References

Adebisi, N., Balogun, A.-L., Min, T. H., & Tella, A. (2021). Advances in estimating sea level rise: A review of tide gauge, satellite altimetry and spatial data science approaches. *Ocean & Coastal Management*, *208*, 105632.

Alexander, M. (2010). Extratropical air-sea interaction, sea surface temperature variability, and the pacific decadal oscillation. *Climate dynamics: why does climate vary?*, *189*, 123–148.

Alvera-Azcárate, A., Barth, A., Sirjacobs, D., Lenartz, F., & Beckers, J.-M. (2011). Data interpolating empirical orthogonal functions (dineof): a tool for geophysical data analyses. *Mediterranean Marine Science*, 5–11.

Alves, D. (2007). Aquaculture in rhode island. In *2007 yearly status report, coastal resource management council.*

Attivissimo, F., Savino, M., & Trotta, A. (2000). A study on nonlinear averagings to perform the characterization of power spectral density estimation algorithms. *IEEE Transactions on Instrumentation and Measurement*, *49*(5), 1036–1042.

Barlage, M. J., Richards, P. L., Sousounis, P. J., & Brenner, A. J. (2002). Impacts of climate change and land use change on runoff from a great lakes watershed. *Journal of Great Lakes Research*, *28*(4), 568–582.

Barnes, B. B., & Hu, C. (2016). Island building in the south china sea: detection of turbidity plumes and artificial islands using landsat and modis data. *Scientific Reports*, *6*(1), 1–12.

Beckers, J. M., & Rixen, M. (2003, December). EOF Calculations and Data Filling from Incomplete Oceanographic Datasets*. *Journal of Atmospheric and Oceanic Technology*, *20*(12), 1839–1856. Retrieved 2022-12-05, from `http://journals.ametsoc.org/doi/10.1175/1520-0426(2003)020<1839:ECADFF>2.0.CO;2` doi: 10.1175/1520-0426(2003)020⟨1839:ECADFF⟩2.0.CO;2

Benoit, J., & Fox-Kemper, B. (2021). Contextualizing thermal effluent impacts in narragansett bay using landsat-derived surface temperature. *Frontiers in Marine Science*, *8*, 705204.

Bertram, D. F., Mackas, D. L., & McKinnell, S. M. (2001). The seasonal cycle revisited: interannual variation and ecosystem consequences. *Progress in Oceanography*, *49*(1-4), 283–307.

Bowers, D., & Brubaker, J. (2021). Providential tides: the double low water of narragansett bay. *Estuaries and Coasts*, *44*(1), 44–53.

Brand, M. (2002). Incremental singular value decomposition of uncertain data with missing values. In *Computer vision—eccv 2002: 7th european conference on computer vision copenhagen, denmark, may 28–31, 2002 proceedings, part i 7* (pp. 707–720).

Bretthorst, G. L. (2001). Generalizing the lomb-scargle periodogram. In *Aip conference proceedings* (Vol. 568, pp. 241–245).

Brown, C. A., Sharp, D., & Collura, T. C. M. (2016). Effect of climate change on water temperature and attainment of water temperature criteria in the yaquina estuary, oregon (usa). *Estuarine, Coastal and Shelf Science*, *169*, 136–146.

Byron, C., Link, J., Costa-Pierce, B., & Bengtson, D. (2011). Calculating ecological carrying capacity of shellfish aquaculture using mass-balance modeling: Narragansett bay, rhode island. *Ecological Modelling*, *222*(10), 1743–1755.

Carney, M. A. (1997). *Surface temperatures in narragansett bay: Seasonal dynamics and anthropogenic effects* (Unpublished doctoral dissertation). Citeseer.

Chen, J.-M., & Harr, P. A. (1993). Interpretation of extended empirical orthogonal function (eeof) analysis. *Monthly weather review*, *121*(9), 2631–2636.

Cheng, P., Valle-Levinson, A., & de Swart, H. E. (2011). A numerical study of residual circulation induced by asymmetric tidal mixing in tidally dominated estuaries. *Journal of Geophysical Research: Oceans*, *116*(C1).

Cloern, J. E., Abreu, P. C., Carstensen, J., Chauvaud, L., Elmgren, R., Grall, J., ... others (2016). Human activities and climate variability drive fast-paced change across the world's estuarine–coastal ecosystems. *Global change biology*, *22*(2), 513–529.

Cocco, V., Joos, F., Steinacher, M., Frölicher, T. L., Bopp, L., Dunne, J., ... others (2013). Oxygen and indicators of stress for marine life in multi-model global warming projections. *Biogeosciences*, *10*(3), 1849–1868.

Cruz, C., Hedderley, D., & Fletcher, G. (2015). Long-term study of vibrio parahaemolyticus prevalence and distribution in new zealand shellfish. *Applied and environmental microbiology*, *81*(7), 2320–2327.

Dalrymple, R. W., Mackay, D. A., Ichaso, A. A., & Choi, K. S. (2012). Processes, morphodynamics, and facies of tide-dominated estuaries. *Principles of tidal sedimentology*, 79–107.

Dalton, T., Thompson, R., & Jin, D. (2010). Mapping human dimensions in marine spatial planning and management: An example from narragansett bay, rhode island. *Marine Policy*, *34*(2), 309–319.

De Boer, P. L., Oost, A., & Visser, M. (1989). The diurnal inequality of the tide as a parameter for recognizing tidal influences. *Journal of Sedimentary Research*, *59*(6), 912–921.

Deser, C., Alexander, M. A., Xie, S.-P., & Phillips, A. S. (2010). Sea surface temperature variability: Patterns and mechanisms. *Annual review of marine science*, *2*, 115–143.

Fassoni-Andrade, A. C., Durand, F., Moreira, D., Azevedo, A., dos Santos, V. F., Funi, C., & Laraque, A. (2021). Comprehensive bathymetry and intertidal topography of the amazon estuary. *Earth System Science Data Discussions*, *2021*, 1–27.

Fisher, J. I., & Mustard, J. F. (2004). High spatial resolution sea surface climatology from landsat thermal infrared data. *Remote Sensing of Environment*, *90*(3), 293–307.

Fournier, S., Chapron, B., Salisbury, J., Vandemark, D., & Reul, N. (2015). Comparison of spaceborne measurements of sea surface salinity and colored detrital matter in the amazon plume. *Journal of Geophysical Research: Oceans*, *120*(5), 3177–3192.

Fox, M. F., Kester, D. R., Andrews, J. E., Magnuson, A., & Zoski, C. G. (2000). Seasonal warming of narragansett bay and rhode island sound in 1997: Advanced very high resolution radiometer sea surface temperature and in situ measurements. *Journal of Geophysical Research: Oceans*, *105*(C9), 22071–22082.

Fox, M. F., Kester, D. R., & Yoder, J. A. (2005). Spatial and temporal distributions of surface temperature and chlorophyll in the gulf of maine during 1998 using seawifs and avhrr imagery. *Marine Chemistry*, *97*(1-2), 104–123.

Fox-Kemper, B. (2004, March). Wind-driven barotropic gyre II: Effects of eddies and low interior viscosity. *Journal of Marine Research*, *62*(2), 195–232. Retrieved 2022-11-28, from `http://www.ingentaselect.com/rpsv/cgi-bin/cgi?ini=xref&body=linker&reqdoi=10.1357/002224004774201690` doi: 10.1357/002224004774201690

Fu, J., Chen, C., Guo, B., Chu, Y., & Zheng, H. (2020). A split-window method to retrieving sea surface temperature from landsat 8 thermal infrared remote sensing data in offshore waters. *Estuarine, Coastal and Shelf Science*, *236*, 106626.

Garrett, C., Keeley, J., & Greenberg, D. (1978). Tidal mixing versus thermal stratification in the bay of fundy and gulf of maine. *Atmosphere-ocean*, *16*(4), 403–423.

Geyer, W. R., & MacCready, P. (2014). The estuarine circulation. *Annual review of fluid mechanics*, *46*, 175–197.

Glynn, E. F., Chen, J., & Mushegian, A. R. (2006). Detecting periodic patterns in unevenly spaced gene expression time series using lomb–scargle periodograms. *Bioinformatics*, *22*(3), 310–316.

Goetz, S. J., Baccini, A., Laporte, N. T., Johns, T., Walker, W., Kellndorfer, J., ... Sun, M. (2009). Remote sensing of environment. *Advances in remote sensing of tropical forests*, *113*, 1013-1026.

Guo, Z., Furtado, K., Zhou, T., Larson, V. E., & Zhang, L. (2022). A positive low cloud–sea surface temperature feedback in the east asian marginal seas during el niño mature winters and their following spring. *Journal of Climate*, *35*(24), 8169–8187.

Hannachi, A., Jolliffe, I. T., & Stephenson, D. B. (2007). Empirical orthogonal functions and related techniques in atmospheric science: A review. *International Journal of Climatology: A Journal of the Royal Meteorological Society*, *27*(9), 1119–1152.

Hansen, M. C., Potapov, P. V., Moore, R., Hancher, M., Turubanova, S. A., Tyukavina, A., ... others (2013). High-resolution global maps of 21st-century forest cover change. *science*, *342*(6160), 850–853.

Harrison, J., Nelson, K., Morcrette, H., Morcrette, C., Preston, J., Helmer, L., ... Wagley, S. (2022). The increased prevalence of vibrio species and the first reporting of vibrio jasicida and vibrio rotiferianus at uk shellfish sites. *Water Research*, *211*, 117942.

Heath, M. R., Neat, F. C., Pinnegar, J. K., Reid, D. G., Sims, D. W., & Wright, P. J. (2012). Review of climate change impacts on marine fish and shellfish around the uk and ireland. *Aquatic Conservation: Marine and Freshwater Ecosystems*, *22*(3), 337–367.

Hernroth, B. E., & Baden, S. P. (2018). Alteration of host-pathogen interactions in the wake of climate change–increasing risk for shellfish associated infections? *Environmental research*, *161*, 425–438.

Hu, W., Wang, Y., Dong, P., Zhang, D., Yu, W., Ma, Z., ... others (2020). Predicting potential mangrove distributions at the global northern distribution margin using an ecological niche model: Determining conservation and reforestation involvement. *Forest Ecology and Management*, *478*, 118517.

Hurrell, J. W., & Deser, C. (2010). North atlantic climate variability: the role of the

north atlantic oscillation. *Journal of marine systems*, *79*(3-4), 231–244.
Ibrahim, I., & Samah, A. A. (2011). Preliminary study of urban heat island: Measurement of ambient temperature and relative humidity in relation to landcover in kuala lumpur. In *2011 19th international conference on geoinformatics* (pp. 1–5).
Jaelani, L. M., & Alfatinah, A. (2017). Sea surface temperature mapping at medium scale using landsat 8-tirs satellite image. *IPTEK Journal of Proceedings Series*, *3*(6).
Jay, D. A., & Musiak, J. D. (1996). Internal tidal asymmetry in channel flows: Origins and consequences. *Mixing in estuaries and coastal seas*, *50*, 211–249.
Jeong, D.-i., Park, K.-h., & Song, B.-g. (2016). A comparison between in-situ pet and envi-met pet for evaluating outdoor thermal comfort. *KIEAE Journal*, *16*(1), 11–19.
Johnson, D. H. (2006). Signal-to-noise ratio. *Scholarpedia*, *1*(12), 2088.
Kennedy, V. S. (1990). Anticipated effects of climate change on estuarine and coastal fisheries. *Fisheries*, *15*(6), 16–24.
Kennish, M. J. (2019). *Ecology of estuaries: anthropogenic effects*. CRC press.
Kilpatrick, K., Podesta, G., & Evans, R. (2001). Overview of the noaa/nasa advanced very high resolution radiometer pathfinder algorithm for sea surface temperature and associated matchup database. *Journal of Geophysical Research: Oceans*, *106*(C5), 9179–9197.
Kincaid, C. (2006). The exchange of water through multiple entrances to the mount hope bay estuary. *Northeastern Naturalist*, 117–144.
Leal Filho, W., Nagy, G. J., Martinho, F., Saroar, M., Erache, M. G., Primo, A. L., ... Li, C. (2022). Influences of climate change and variability on estuarine ecosystems: an impact study in selected european, south american and asian countries. *International Journal of Environmental Research and Public Health*, *19*(1), 585.
Li, C., Li, X., Zhang, G., Boswell, K. M., Kimball, M. E., Shen, D., & Lin, J. (2017). Estuarine plume: A case study by satellite sar observations and in situ measurements. *IEEE Transactions on Geoscience and Remote Sensing*, *55*(4), 2276–2287.
Li, L., Wang, Y., & Liu, D. (2021). Phytoplankton shifts in the central bohai sea over the last 250 years reflect eutrophication and input from the yellow river. *Ecological Indicators*, *126*, 107676.
Li, X., Li, Z., Feng, R., Luo, S., Zhang, C., Jiang, M., & Shen, H. (2019). Generating high-quality and high-resolution seamless satellite imagery for large-scale urban regions. *Remote Sensing*, *12*(1), 81.
Lindquist, E., Hansen, M., Roy, D. P., & Justice, C. (2008). The suitability of decadal image data sets for mapping tropical forest cover change in the democratic republic of congo: implications for the global land survey. *International Journal of Remote Sensing*, *29*(24), 7269–7275.
Lloyd, D. T., Abela, A., Farrugia, R. A., Galea, A., & Valentino, G. (2021). Optically enhanced super-resolution of sea surface temperature using deep learning. *IEEE Transactions on Geoscience and Remote Sensing*, *60*, 1–14.
MacDonald, D. G. (2006). Estimating an estuarine mixing and exchange ratio from boundary data with application to mt. hope bay (massachusetts/rhode island). *Estuarine, Coastal and Shelf Science*, *70*(1-2), 326–332.
Mackenzie, C. L., Lynch, S. A., Culloty, S. C., & Malham, S. K. (2014). Future oceanic warming and acidification alter immune response and disease status in a commercial shellfish species, mytilus edulis l. *PLoS One*, *9*(6), e99712.
McGrath, R., Lynch, P., Dunne, S., Hanafin, J., Nishimura, E., Nolan, P., ... others (2008). Ireland in a warmer world: scientific predictions of the irish climate in the twenty-first century.
McLusky, D. S., Bryant, V., & Campbell, R. (1986). The effects of temperature and

salinity on the toxicity of heavy metals to marine and estuarine invertebrates. *Oceanography and Marine Biology Annual Review*, *24*, 481–520.

McPherson, J. M., Jetz, W., & Rogers, D. J. (2006). Using coarse-grained occurrence data to predict species distributions at finer spatial resolutions—possibilities and limitations. *Ecological Modelling*, *192*(3-4), 499–522.

Metzler, M. D., & Malila, W. A. (1985). Characterization and comparison of landsat-4 and landsat-5 thematic mapper data. *Photogrammetric Engineering and Remote Sensing*, *51*(9), 1315–1330.

Mills, K. E., Pershing, A. J., Brown, C. J., Chen, Y., Chiang, F.-S., Holland, D. S., ... others (2013). Fisheries management in a changing climate: lessons from the 2012 ocean heat wave in the northwest atlantic. *Oceanography*, *26*(2), 191–195.

Minnett, P., Alvera-Azcárate, A., Chin, T., Corlett, G., Gentemann, C., Karagali, I., ... others (2019). Half a century of satellite remote sensing of sea-surface temperature. *Remote Sensing of Environment*, *233*, 111366.

Mustard, J. F., Swanson, C., & Deacutis, C. (2001). Narragansett bay from space: A perspective for the 21st century.

Navarra, A., & Simoncini, V. (2010). *A guide to empirical orthogonal functions for climate data analysis*. Springer Science & Business Media.

Nidzieko, N. J. (2010). Tidal asymmetry in estuaries with mixed semidiurnal/diurnal tides. *Journal of Geophysical Research: Oceans*, *115*(C8).

Nixon, S. W., Granger, S., & Buckley, B. (2003). The warming of narragansett bay. *41 N*, *2*(1), 19–20.

Oczkowski, A., McKinney, R., Ayvazian, S., Hanson, A., Wigand, C., & Markham, E. (2015). Preliminary evidence for the amplification of global warming in shallow, intertidal estuarine waters. *PLoS One*, *10*(10), e0141529.

Oviatt, C., Keller, A., & Reed, L. (2002). Annual primary production in narragansett bay with no bay-wide winter–spring phytoplankton bloom. *Estuarine, Coastal and Shelf Science*, *54*(6), 1013–1026.

Oviatt, C., Olsen, S., Andrews, M., Collie, J., Lynch, T., & Raposa, K. (2003). A century of fishing and fish fluctuations in narragansett bay. *Reviews in Fisheries Science*, *11*(3), 221–242.

O'carroll, A. G., Armstrong, E. M., Beggs, H. M., Bouali, M., Casey, K. S., Corlett, G. K., ... others (2019). Observational needs of sea surface temperature. *Frontiers in Marine Science*, *6*, 420.

Paden, C. A., Abbott, M. R., & Winant, C. D. (1991). Tidal and atmospheric forcing of the upper ocean in the gulf of california: 1. sea surface temperature variability. *Journal of Geophysical Research: Oceans*, *96*(C10), 18337–18359.

Paxton, C. W., Baria, M. V. B., Weis, V. M., & Harii, S. (2016). Effect of elevated temperature on fecundity and reproductive timing in the coral acropora digitifera. *Zygote*, *24*(4), 511–516.

Pershing, A. J., Alexander, M. A., Brady, D. C., Brickman, D., Curchitser, E. N., Diamond, A. W., ... others (2021). Climate impacts on the gulf of maine ecosystem: A review of observed and expected changes in 2050 from rising temperatures. *Elem Sci Anth*, *9*(1), 00076.

Pfeiffer-Herbert, A., Kincaid, C., Bergondo, D., & Pockalny, R. (2015). Dynamics of wind-driven estuarine-shelf exchange in the narragansett bay estuary. *Continental Shelf Research*, *105*, 42–59.

Piccioni, F., Casenave, C., Lemaire, B. J., Le Moigne, P., Dubois, P., & Vinçon-Leite, B. (2021). The thermal response of small and shallow lakes to climate change: new insights from 3d hindcast modelling. *Earth System Dynamics*, *12*(2), 439–456.

Pourkerman, M., Marriner, N., Amjadi, S., Lak, R., Hamzeh, M., Mohammadpor, G., ... Shah-Hosseini, M. (2023). The impacts of persian gulf water and ocean-atmosphere interactions on tropical cyclone intensification in the arabian sea. *Marine Pollution Bulletin*, *188*, 114553.

Priyanka, K., Sarangi, R. K., Elangovan, M., Jaiganesh, S. N., Utthamapandian, U., & Saravanakumar, A. (2021). Phytoplankton and nutrients abundance in relation to ekman mass transport in the arabian sea. *Regional Studies in Marine Science*, *48*, 101984.

Raposa, K. B. (2009). Ecological geography of narragansett bay. *An Ecological Profile of the Narragansett Bay National Estuarine Research Reserve*, 77–88.

Reddy, G. O. (2018). Satellite remote sensing sensors: principles and applications. *Geospatial technologies in land resources mapping, monitoring and management*, 21–43.

Rivas-Fandiño, P., Acuña-Alonso, C., Novo, A., Pacheco, F. A. L., & Álvarez, X. (2023). Assessment of high spatial resolution satellite imagery for monitoring riparian vegetation: riverine management in the smallholding. *Environmental Monitoring and Assessment*, *195*(1), 81.

Roy, D. P., Ju, J., Kline, K., Scaramuzza, P. L., Kovalskyy, V., Hansen, M., ... Zhang, C. (2010). Web-enabled landsat data (weld): Landsat etm+ composited mosaics of the conterminous united states. *Remote Sensing of Environment*, *114*(1), 35–49.

Roy, D. P., Kovalskyy, V., Zhang, H., Vermote, E. F., Yan, L., Kumar, S., & Egorov, A. (2016). Characterization of landsat-7 to landsat-8 reflective wavelength and normalized difference vegetation index continuity. *Remote sensing of Environment*, *185*, 57–70.

Rubinetti, S., Zanchettin, D., Gazzola, K., Papa, A., & Rubino, A. (2022). Mid-xix century estuary sst time series recorded in the venice lagoon. *Climate*, *10*(10), 155.

Ryan, W. B. F., Carbotte, S. M., Coplan, J., O'Hara, S., Melkonian, A., Arko, R., ... Zemsky, R. (2009). Global multi-resolution topography (gmrt) synthesis data set. *Geochemistry, Geophysics, Geosystems*, *10*, Q03014. doi: 10.1029/2008GC002332

Saba, V. S., Griffies, S. M., Anderson, W. G., Winton, M., Alexander, M. A., Delworth, T. L., ... others (2016). Enhanced warming of the n orthwest a tlantic o cean under climate change. *Journal of Geophysical Research: Oceans*, *121*(1), 118–132.

Sandau, R., Brieß, K., & D'Errico, M. (2010). Small satellites for global coverage: Potential and limits. *ISPRS Journal of photogrammetry and Remote Sensing*, *65*(6), 492–504.

Sane, A., Fox-Kemper, B., & Ullman, D. (2023, May). Internal vs forced variability metrics for geophysical flows using information theory. *Journal of Geophysical Research–Oceans*. Retrieved from `https://fox-kemper.com/pubs/pdfs/SaneFox-Kemper23.pdf` (Submitted)

Sathyendranath, S., Brewin, R. J., Brockmann, C., Brotas, V., Calton, B., Chuprin, A., ... others (2019). An ocean-colour time series for use in climate studies: the experience of the ocean-colour climate change initiative (oc-cci). *Sensors*, *19*(19), 4285.

Schneider, K., & Mauser, W. (1996). Processing and accuracy of landsat thematic mapper data for lake surface temperature measurement. *International Journal of Remote Sensing*, *17*(11), 2027-2041. doi: 10.1080/01431169608948757

Scrosati, R. A., Ellrich, J. A., & Freeman, M. J. (2020). Half-hourly changes in intertidal temperature at nine wave-exposed locations along the atlantic canadian coast: a 5.5-year study. *Earth System Science Data*, *12*(4), 2695–2703.

Simionato, C. G., Tejedor, M. L. C., Campetella, C., Guerrero, R., & Moreira, D. (2010). Patterns of sea surface temperature variability on seasonal to subannual scales at and offshore the río de la plata estuary. *Continental Shelf Research*, *30*(19), 1983–1997.

Simpson, J., Souza, A., & Lavin, M. (1994). *Tidal mixing in the gulf of california.*

John Wiley and Sons.

Smith, L. M., Whitehouse, S., & Oviatt, C. A. (2010). Impacts of climate change on narragansett bay. *Northeastern Naturalist*, *17*(1), 77–90.

Spaulding, M. L., & Swanson, C. (2008). Circulation and transport dynamics in narragansett bay. In *Science for ecosystem-based management: Narragansett bay in the 21st century* (pp. 233–279). Springer.

Tarantino, E. (2012). Monitoring spatial and temporal distribution of sea surface temperature with tir sensor data. *Ital. J. Remote Sens*, *44*(1), 97–107.

Turner, W., Rondinini, C., Pettorelli, N., Mora, B., Leidner, A. K., Szantoi, Z., ... others (2015). Free and open-access satellite data are key to biodiversity conservation. *Biological Conservation*, *182*, 173-176.

VanderPlas, J. T. (2018). Understanding the lomb–scargle periodogram. *The Astrophysical Journal Supplement Series*, *236*(1), 16.

Vanhellemont, Q., Brewin, R. J., Bresnahan, P. J., & Cyronak, T. (2022). Validation of landsat 8 high resolution sea surface temperature using surfers. *Estuarine, Coastal and Shelf Science*, *265*, 107650.

Vroom, J., Van der Wegen, M., Martyr-Koller, R. C., & Lucas, L. (2017). What determines water temperature dynamics in the san francisco bay-delta system? *Water Resources Research*, *53*(11), 9901–9921.

Wall, M. E., Rechtsteiner, A., & Rocha, L. M. (2003). Singular value decomposition and principal component analysis. In *A practical approach to microarray data analysis* (pp. 91–109). Springer.

Wang, Y., Xu, H., & Li, M. (2021). Long-term changes in phytoplankton communities in china's yangtze estuary driven by altered riverine fluxes and rising sea surface temperature. *Geomorphology*, *376*, 107566.

Weare, B. C., & Nasstrom, J. S. (1982). Examples of extended empirical orthogonal function analyses. *Monthly Weather Review*, *110*(6), 481–485.

Welch, R., Jordan, T., & Ehlers, M. (1985). Comparative evaluations of the geodetic accuracy and cartographic potential of landsat-4 and landsat-5 thematic mapper image data. *Photogrammetric engineering and remote sensing*, *51*(9), 1249–1262.

Wells, J. T. (1995). Tide-dominated estuaries and tidal rivers. In *Developments in sedimentology* (Vol. 53, pp. 179–205). Elsevier.

Wojtasiewicz, B., Hardman-Mountford, N. J., Antoine, D., Dufois, F., Slawinski, D., & Trull, T. W. (2018). Use of bio-optical profiling float data in validation of ocean colour satellite products in a remote ocean region. *Remote Sensing of Environment*, *209*, 275–290.

Wulder, M. A., Loveland, T. R., Roy, D. P., Crawford, C. J., Masek, J. G., Woodcock, C. E., ... others (2019). Current status of landsat program, science, and applications. *Remote sensing of environment*, *225*, 127–147.

Wulder, M. A., White, J. C., Masek, J. G., Dwyer, J., & Roy, D. P. (2011). Continuity of landsat observations: Short term considerations. *Remote Sensing of Environment*, *115*(2), 747–751.

Xu, Y., Wu, Y., Xiu, P., Ge, J., & Zhang, J. (2022). Unraveling environmental drivers of chlorophyll seasonal and interannual variability in the east china sea. *Frontiers in Marine Science*, *9*, 951395.

Zeng, S., Lei, S., Li, Y., Lyu, H., Xu, J., Dong, X., ... Li, J. (2020). Retrieval of secchi disk depth in turbid lakes from goci based on a new semi-analytical algorithm. *Remote Sensing*, *12*(9), 1516.

Zhao, J., Temimi, M., & Ghedira, H. (2017). Remotely sensed sea surface salinity in the hyper-saline arabian gulf: Application to landsat 8 oli data. *Estuarine, Coastal and Shelf Science*, *187*, 168–177.